CHALMERS
UNIVERSITY OF TECHNOLOGY

Investigation of the near-wake flow topology of a simplified heavy vehicle using PANS simulations

Citation for the original published paper (version of record):
Rao, A., Minelli, G., Zhang, J. et al (2018). Investigation of the near-wake flow topology of a simplified heavy vehicle using PANS
simulations. Journal of Wind Engineering and Industrial Aerodynamics, 183: 243-272.
http://dx.doi.org/10.1016/j.jweia.2018.09.019

Journal of Wind Engineering & Industrial Aerodynamics 183 (2018) 243–272

Contents lists available at ScienceDirect

Journal of Wind Engineering & Industrial Aerodynamics

journal homepage: www.elsevier.com/locate/jweia

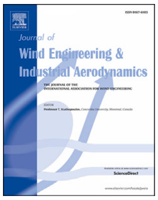

Investigation of the near-wake flow topology of a simplified heavy vehicle using PANS simulations

Anirudh N. Rao [a,*], Guglielmo Minelli [a], Jie Zhang [a], Branislav Basara [b], Siniša Krajnović [a,*]

[a] Department of Mechanics and Maritime Sciences, Chalmers University of Technology, Göteborg, 41296, Sweden
[b] AVL List GmbH, Advanced Simulation Technologies, Hans-List-Platz 1, 8020, Graz, Austria

ARTICLE INFO

Keywords:
Heavy vehicles
Wakes
Bi-stability
Hybrid RANS-LES

ABSTRACT

The near-wake flow topology of a ground transportation system (GTS) is investigated using partially-averaged Navier–Stokes (PANS) simulations at $Re = 2.7 \times 10^4$. Recent numerical investigations for the GTS model using large eddy simulations (LES) showed an anti-symmetric flow topology (flow state II) in the vertical midplane compared to that observed in previous experimental studies (flow state I). The geometrical configuration of the GTS permits bi-stable behaviour, and the realisation of each of the two flow states, which are characterised by an asymmetrical flow topology, is achieved by varying the differencing scheme for the convective flux in the PANS simulations; AVL SMART schemes predict flow state I, while central differencing scheme (CDS) predicts flow state II. When the GTS model was placed away from the ground plane, the AVL SMART scheme fails to predict the flow asymmetry resulting in a pair of symmetrical vortices in the vertical midplane, while flow state II topology is observed when CDS is used. The switch from flow state I (II) to flow state II (I) is achieved by changing the numerical scheme from AVL SMART (CDS) to CDS (AVL SMART), with an intermediate transient-symmetric (TS) state being observed during the switching process. The numerical scheme in the PANS simulations thus plays a critical role in determining the initial flow topology in the near wake of the GTS.

1. Introduction

In this study, we use PANS simulations to predict the near-wake flow topology of a generic squareback bluff body – the GTS model. The GTS model is representative of a truck and a trailer with no intermediate gap, and is commonly used model in the transportation industry to investigate the aerodynamics of heavy vehicles. While a more detailed description of the near-wake flow topology of heavy vehicles has been presented in Rao et al. (2018b), where well-resolved LES were undertaken on a simplified GTS model; a brief description of the literature reviewed is presented here.

Recent experimental investigations at $Re = 2.7 \times 10^4$ by McArthur et al. (2016) has shown that the flow topology in the vertical midplane of the GTS model is invariant over a large range of Reynolds numbers (Re, defined as the ratio of the inertial to the viscous forces), with a near identical flow topology being observed at $Re = 2 \times 10^6$ (Storms et al. (2001), Croll et al. (1996)). The mean flow topology in this plane is asymmetrical, and consists of a large triangular-shaped vortex on one side, with an elliptical-shaped vortex located opposite to it, and a pair of counter-rotating vortices is observed in the lateral midplane (also see McArthur et al. (2016) and Rao et al. (2018b) for a detailed description of the flow topology). Previous studies using RANS (Reynolds-averaged Navier–Stokes) turbulence models have failed to accurately predict the asymmetrical flow topology in the vertical midplane (Salari et al. (2004), Roy et al. (2006), Ghias et al. (2008)). LES for a truncated GTS model by Ortega et al. (2004) and detached eddy simulations (DES) by Unaune et al. (2005) showed a flow topology in the vertical midplane which is anti-symmetric to that observed in the experiments, while the URANS (unsteady Reynolds-averaged Navier–Stokes) $k-\varepsilon$ RNG turbulence model used by Gunes (2010) showed a flow topology similar to the experimental studies at $Re = 2 \times 10^6$. With the flow topology remaining invariant over a wide range of Reynolds numbers, well-resolved LES were undertaken by Rao et al. (2018b) for a simplified GTS model, with modifications to the frontal A-pillars to obtain solutions on a purely hexahedral mesh, replicating the work of McArthur et al. (2016). The mean flow topology in the vertical midplane was anti-symmetric to that observed in McArthur et al. (2016) for three meshes of increasing spatial resolution, and the flow topology was also insensitive to small yaw angles of up to 2.5° (also see Gentile et al. (2017), Volpe et al. (2014a)). Furthermore, when the GTS model was placed at large distances from the

---

* Corresponding authors.
E-mail addresses: anirudh.rao@chalmers.se (A.N. Rao), sinisa.krajnovic@chalmers.se (S. Krajnović).

https://doi.org/10.1016/j.jweia.2018.09.019
Received 22 June 2018; Received in revised form 5 September 2018; Accepted 21 September 2018

ground plane at $1.1H$, the flow topology was identical to that observed at a lower gap height of $0.14H$, where, H is the height of the GTS model (Grandemange et al. (2013a), McArthur et al. (2016), Castelain et al. (2018)). It may be noted that the symmetry-breaking flow states in the near wake occur independently of the frontal shape of the bluff body and any planar symmetry that the body may possess. Bi-stable flow has been observed in the lateral midplane of a squareback body which is not symmetrical about the lateral midplane; for instance, the squareback Windsor model (see Pavia et al. (2017), Pavia and Passmore (2018), Perry et al. (2016)) which has the same overall dimensions of the idealised car model - the *Ahmed body* (see Ahmed et al. (1984)), but a more realistic frontal shape (Howell and Le Good (2008)), and also in the air-wake of simplified frigate models (see Herry et al. (2011), Zhang et al. (2018)).

These studies indicate that two flow solutions are possible in the wake of the GTS, and the switching between two flow states is usually observed in the experimental studies, where the phenomenon is referred to as bi-stability (or the random occurrence of the bi-stable states/bi-modal solutions), and has been observed in the wake of squareback bluff bodies (Volpe et al. (2014a), Volpe et al. (2015), Grandemange et al. (2013a), Herry et al. (2011), Grandemange et al. (2013b), Lahaye et al. (2014), Grandemange et al. (2014), Lucas et al. (2017), Evrard et al. (2016), Varon et al. (2017), Eulalie et al. (2017), Bonnavion and Cadot (2018) and others). Only one of the two possible flow states is usually observed in numerical simulations, which are usually performed for a finite time as compared to experimental studies, which are carried out for much longer time periods. It may be recalled that the height-to-width ratio of the GTS (1.392) is approximately equal to the width-to-height ratio of the squareback Ahmed body (1.35), thus indicating that the aspect ratio of the bluff body is a critical parameter in determining the occurrence of bi-stable flow states (Grandemange et al. (2013a), McArthur et al. (2016)). While the bi-stable states observed in the wake of squareback Ahmed body occur in the lateral midplane, the two flow states in the GTS wake are observed in the vertical midplane; flow state I in McArthur et al. (2016) and Gunes (2010), and flow state II in Schmidt et al. (2018), Rao et al. (2018b), Ortega et al. (2004) and Unaune et al. (2005). The wake asymmetry (and the resulting bi-stable flow state) was found to originate at low Reynolds numbers for a squareback Ahmed body, where the flow transitions from a steady asymmetric flow state to an unsteady asymmetric flow state at $Re \simeq 410$ via an imperfect supercritical bifurcation (Grandemange et al. (2012), Cadot et al. (2015)), and is observed at Reynolds numbers well into the turbulent region of flow at $Re \simeq 9.5 \times 10^4$. More recently, sensitivity analysis and exploration of the wake dynamics of the squareback Ahmed body studies has garnered much interest, and drag reduction strategies such as flow control (active/passive or a combination of both) have been applied to manipulate the wake to a low drag state (also see Li et al. (2016), Perry et al. (2016), Lucas et al. (2017), Grandemange et al. (2015), Evstafyeva et al. (2017), Rouméas et al. (2009), Bruneau et al. (2010), Li (2017), Li et al. (2017), Barros et al. (2017b), Brackston et al. (2016), Rigas et al. (2017) and others). The results from such analyses can be directly applied to the wake of the GTS; thereby, leading to cost savings and reduction in the carbon footprint for the transport industry (El-Alti et al. (2016), Lo and Kontis (2017), Haff et al. (2017)).

While direct numerical simulations (DNS) are used to accurately predict the flow at low Reynolds numbers, they require significant computational effort/resources to resolve the flow structures at higher Reynolds numbers. For such cases, RANS turbulence closure models are used, and these provide a mean (ensemble-averaged) flow field, by separating the mean and fluctuating components of the Navier–Stokes (N-S) equations. URANS incorporates the time-dependent terms of the N-S equations, and captures only the large deterministic structures while suppressing the finer scale structures (Davidson (2018), Salim and Ong (2013), Girimaji et al. (2005)). LES use a filter (which usually depends on the mesh resolution) to resolve the largest scales and modelling the finest scales using various subgrid scale (SGS) models (also see Sagaut (2006), Minguez et al. (2008)), and are computationally less expensive than DNS, but more than RANS (Zhiyin (2015)). Thus, the need to have bridging models arise, where the SGS models go smoothly from URANS to DNS solution with increasing spatial resolution (Speziale (1997)). Several zonal and non-zonal hybrid turbulence models have been proposed such as DES (Spalart et al. (1997)) and its variants - Delayed DES (Spalart et al. (2006)) and Improved DDES (Shur et al. (2008)), Embedded LES (ELES) (Mathey et al. (2006)), Scale Adaptive Simulations (SAS) (Menter and Egorov (2010)), and PANS (Girimaji et al. (2005), Girimaji and Abdol-Hamid (2005), Basara et al. (2011)). The zonal methods separate the near wall region (resolved using a RANS model) and the outer regions (where LES is used) by a distinct interface (also see Jakirlic and Maduta (2015)), while the non-zonal methods seamlessly bridge the two regions. The comparison/assessment between various turbulence models for canonical/simplistic bluff bodies has been widely reported (Guilmineau et al. (2017), Maleki et al. (2017), Serre et al. (2013) and others); more realistic geometries have also been assessed (Wang et al. (2017), Jakirlic et al. (2017a), Jakirlic et al. (2017b), Jakirlic et al. (2014), Ashton et al. (2016) and Pereira et al. (2018a)). It may be noted that different methodologies/closure models for turbulence have been proposed over the past few years, and only the major models are mentioned here.

Here, an assessment of the PANS turbulence modelling approach on a simplified tractor-trailer geometry - the GTS model, is carried out on grids that are deemed capable for a well-resolved LES (see Rao et al. (2018b)). Investigation of the influence of numerical schemes in solvers has become a common practice in computational fluid dynamic analysis (Basara et al. (2018), Robertson et al. (2015), Adedoyin et al. (2015), Baxevanou and Vlachos (2004), Sans et al. (2014), Aubin et al. (2004), Nakayama and Vengadesan (2002) and others). Here, the influence of the differencing schemes used for the convective flux on the initial flow topology (first few flow-passes through the domain after transience) which is susceptible to bi-stable solutions in the vertical midplane is investigated for the GTS at gap heights of $0.14H$ and $1.1H$. The remainder of the article is organised as follows: section 2 elucidates the problem setup, and the PANS numerical formulation is briefly described. The flow topology in the vertical midplane obtained with the differencing schemes on grids of increasing spatial resolution, for the incoming flow at zero yaw angle at two gap heights is detailed in section 3.1. The switching between the bi-stable flow states by altering the numerical scheme is presented in section 3.2. The variation of the force coefficients for the various cases investigated is discussed in section 3.3. The main findings of this study are summarised in section 4.

2. Methodology

2.1. Problem setup

The GTS model is a canonical bluff body; with a rounded front edge and an elongated flat section with a square back. The side and bottom edges at the front are curved, and is representative of a truck with a trailer, with no intermediate gap. In order to aid the construction of a hexahedral mesh, the two-dimensional profile of the GTS model in the midplane was extruded to a distance equal to the width of the model. In effect, the A-pillar fillets of the original GTS model were removed, resulting in sharp frontal edges, thereby ensuring a fixed separation point for the flow on the sides of the modified model. This simplification would affect the flow around the model, and the overall drag coefficient. Sitlani and Aung (2006) reported a 46% increase in the drag coefficient for a GTS model with a sharp lower frontal edge as compared to the standard case with the filleted edge. However, the flow topology at the rear of the model was found to be invariant of the frontal shape of the model as seen in the results of Ortega et al. (2004), where an asymmetrical flow topology similar to Storms et al. (2001) was observed in the wake of a truncated GTS model, albeit transposed across the lateral midplane. The schematic of the GTS model used in this study is shown in Fig. 1(a). Two

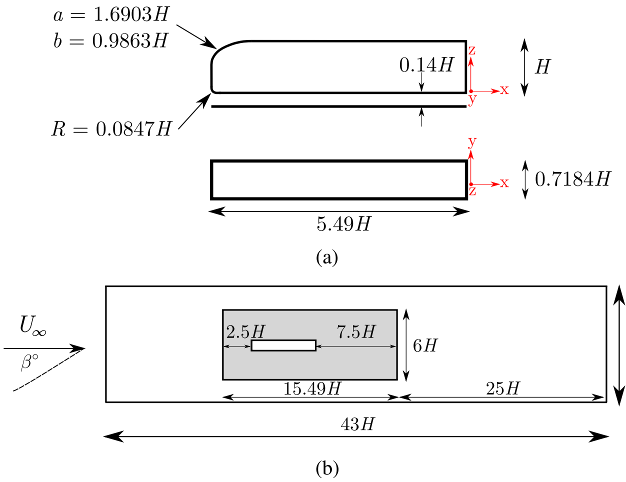

Fig. 1. (Colour online) (a) Schematic of the GTS model showing the major dimensions of the model. The upper frontal shape of the model is elliptical, with the dimensions of the semi-major axis (a) and semi-minor axis (b) shown. The bottom edge at the front of the model is filleted with a radius, R. (b) Schematic of the computational domain in plan view, with the no-slip region shaded in gray. The dimensions of the GTS model and the computational domain are normalised by the height of the GTS, and the incoming flow yaw angle is set to $\beta = 0^{\circ}$. Image reproduced from Rao et al. (2018b).

gap heights are considered in this study; one where the model is placed close to the ground at a height of $0.14H$, and the second case where the model is placed at a height of $1.1H$ above the ground to study the influence of the shape of the model in the absence of ground effect. The incoming flow is set to $\beta = 0^{\circ}$, where β is the yaw angle. The Reynolds number ($Re = U_{\infty}W/\nu$, where ν is the kinematic viscosity of the fluid), defined as ratio of the inertial forces to the viscous forces, is identical to that in the experimental work of McArthur et al. (2016). The inlet velocity was set to $U_{\infty} = 1.2768$ ms^{-1} to obtain a Reynolds number $Re_W \simeq 2.7 \times 10^4$, based on the width (W) of the model. While the width of the GTS is used to define the Reynolds number, other quantities such as distances are normalised by the height (H) of the GTS.

The simplified GTS model is placed at the centre of the computational domain above the ground plane as shown in Fig. 1(b). The origin is located at the midway point of the bottom rear edge of the model. The ground boundary condition used here is set to replicate the experimental work of McArthur et al. (2016), with a slip wall enclosing a no-slip wall. The no-slip wall extends $2.5H$ and $7.5H$ upstream and downstream of the model, respectively, and $3H$ on either side of the model. The inlet and outlet boundaries are at a distance of $18H$ and $25H$ from the origin. The lateral and top boundaries extend $5H$ and $9H$ from the origin, respectively, and are assigned symmetry boundary conditions. The blockage ratio based on the ratio of the frontal areas of the GTS model and the inlet area of the computational domain was $\lesssim$1%. While previous experimental investigations have used cylindrical or streamlined supports, these were not used for the model considered here, thereby leading to unperturbed underbody flow, which is important for the prediction of the bi-stable flow states. The homogeneous Neumann boundary condition is used at the outlet.

The computational domain consisted of purely hexahedral elements, and three meshes of increasing resolution were constructed to investigate the influence of the spatial resolution on the flow topology. For the GTS model at $G/H = 0.14$, the coarse, medium and fine meshes consisted of approximately 3.88, 8.35 and 10.78 million elements, respectively, and for the case where the GTS model is at a height of $1.1H$ above the ground, the computational domain consisted of approximately 9.18 million elements. The hexahedral meshes used in this study are identical to those used in the LES of Rao et al. (2018b). A polyhedral mesh consisting of approximately 5.5 million elements was also used for the PANS investigation of the GTS at a gap height of $0.14H$ (see appendix A for details on the construction and the cross-sectional views of the polyhedral mesh) to investigate the influence of the mesh construction on the flow topology. For all the unsteady cases considered here, a time-step was set to $7.5 \times 10^{-4}s$ to ensure a CFL (Courant-Friedrichs-Lewy) number less than unity around the GTS model. The flow quantities and forces were averaged for five (or more) flow passages after an initial transience of one flow passage (which corresponds to a time-interval of $t \simeq 15.2$s or 20,267 time-steps), which is in line with recent numerical studies on vehicle aerodynamics (see Aljure et al. (2018), Lucas et al. (2017) and Guilmineau et al. (2017)). All simulations reported here with the exception of those in section 3.2 were started from a quiescent condition. The total computational time required for this study exceeded 0.6 million CPU hours.

2.2. Numerical formulation

PANS turbulence closure model is a non-zonal hybrid RANS-LES method that adapts to the spatial resolution of a given mesh to provide solutions between URANS equations and DNS (Ma et al. (2011), Girimaji and Suman (2012)). Two parameters that govern the PANS equations are the ratios of the unresolved to total kinetic energy and the dissipation, f_k and f_{ε}, respectively. While $f_{\varepsilon} = 1$ is assumed (i.e. the unresolved dissipations scales in PANS and URANS model are identical), f_k can take values between zero and unity, depending on the spatial resolution and the ratio of the kinetic energy to its dissipation (Girimaji and Abdol-Hamid (2005), Girimaji (2006)). $f_k = 1$ corresponds to a URANS solution; $f_k = 0$ corresponds to a fully-resolved DNS solution, and for values between zero and one, the flow is partially resolved, while other turbulent structures are modelled (Ma et al. (2011)). The PANS $\zeta - f$ model based on the four equation $k - \varepsilon - \zeta - f$ URANS model of Hanjalić et al. (2004) to improve the near-wall modelling is used here (Basara et al. (2011), Krajnović et al. (2012a)). The PANS equations are discretised using a finite volume solver, AVL FIRE™2014 (AVL (2014)). The results from the PANS simulations in this study are compared to those obtained from the LES of Rao et al. (2018b), which are used as a baseline for comparison. The PANS equations have previously been detailed for a wide range of bluff body flows in Basara et al. (2011), Minelli et al. (2017), Mirzaei et al. (2015), Krajnović et al. (2012b), Jakirlic et al. (2016), Basara (2015b), Minelli et al. (2016), and the LES equations in Östh and Krajnović (2016), Östh et al. (2014), Östh et al. (2010) Krajnović and Lárusson (2012) and others.

The current study focuses on changes to the flow topology brought about by the numerical schemes used for the momentum equations. For the simulations with PANS equations, the second-order accurate AVL SMART (Sharp and Monotonic Algorithm for Realistic Transport) was used for the momentum equations (Pržulj and Basara (2001), Pržulj (2016), Basara (2004), Basara (2015a) and the references therein) in conjunction with MINMOD (MINimum MODulus) for the turbulence equations (also see Harten (1983), Sweby (1984)); while for the LES, a blend of 95% central differencing with 5% first-order upwind scheme (CDS) is used for the convective flux in the momentum equations. Pure central differencing scheme was used for the continuity equation. The SMART scheme first proposed by Gaskell and Lau (1988) was modified to improve the convergence properties, and has been detailed in Pržulj and Basara (2001) (also see Lin and Lin (1997) and Lien and Leschziner (1994)). The MINMOD scheme was found to be more diffusive than the variants of SMART, and has good convergence properties that can deliver second-order accurate solutions on refined grids (Pržulj and Basara (2001), AVL (2014), Basara et al. (2011), Waterson and Deconinck (2007)). Two variants of the AVL SMART scheme are available: AVL SMART Relaxed (ASR) and AVL SMART Bounded (ASB), with the ASB having better convergence properties as compared to ASR. The influence of these two variants of the AVL SMART schemes is also tested, and the velocity profiles in the wake showed negligible difference as seen in

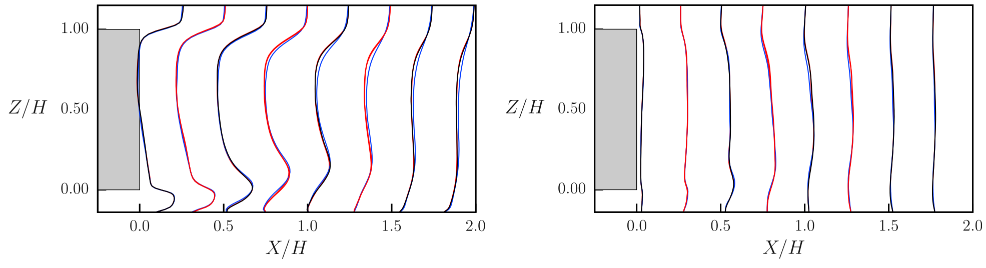

(a) (b)

Fig. 2. (Colour online) Comparison of the velocity profiles in the wake of the GTS model in the vertical midplane. (a) streamwise velocity and (b) vertical velocity. The black, red and blue lines correspond to the medium mesh with ASR, medium mesh with ASB, and fine mesh with ASB, respectively. Flow is from left to right in these images.

Fig. 2. While low Reynolds numbers PANS simulations are usually run using CDS for higher accuracy (Lakshmipathy (2004), Lakshmipathy et al. (2011), Ma et al. (2011)). However, use of CDS can give an appearance that the flow is relatively more unsteady as a result of less damping of the unresolved viscosity, and may lead to the formation of smaller coherent structures and spurious oscillations (Krajnović et al. (2016)), and the use of QUICK (Quadratic Upstream Interpolation for Convective Kinematics) based schemes have also been used at low Reynolds numbers (Verma and Dewan (2018)). Thus, the influence of CDS in PANS for “LES-capable” grids (or grids of adequate spatial resolution) is investigated for the GTS at $G = 0.14H$, and at $G = 1.1H$, for comparison with the AVL SMART schemes.

A blending factor (defined as the proportion of central differencing scheme blend with first order upwind scheme) of 0.95 was used for the convective flux in the LES of Rao et al. (2018b). An increase in the value of the blending factor beyond 0.95 led to the formation of spurious (non-physical) flow structures at the front of the GTS (also see section 5 of Krajnović et al. (2016)). Furthermore, it led to the centres of the vortex cores in the near wake being located closer to the base of the GTS, resulting in an increase in the drag coefficient. Thus, a blending factor of 0.95 used for the PANS - CDS simulations in this study. The number of iterations per time-step was marginally higher for simulations using the CDS as compared to those using the AVL SMART schemes for the first few flow passages through the domain, leading to slightly longer run times for the PANS - CDS simulations. In each simulation, the absolute value of the residuals converged to better than 10^{-6} for the three velocity components, and to 10^{-4} for the pressure.

2.3. Spatial resolution study

The computational grids for the current PANS simulations are identical to that used in the LES of Rao et al. (2018b). For images of the distribution of the elements on the surface of the GTS and around it, the reader is referred to Rao et al. (2018b). Table 1 shows the maximum grid spacing in the three directions. Here, n^+ is the dimensionless wall distance given by $n^+ = nu_\tau/\nu$, where, n is the distance of the first cell height from the wall, and u_τ is the friction velocity. The recommended grid spacing in the streamwise and spanwise directions for LES needs to be within $\Delta s^+ = \Delta s u_\tau/\nu = 50 - 150$, $\Delta l^+ = \Delta l u_\tau/\nu = 15 - 40$, respectively, in order to resolve the near wall structures (see Piomelli and Chasnov (1996)). Here, Δs and Δl are the values of grid spacing in the streamwise and spanwise directions, respectively. These limits are less stringent for PANS simulations, on account of its adaptivity, the grid spacing from the PANS simulations on the medium and fine mesh are well within the recommended values for LES.

Table 1
Details of the computational mesh.

Description	Mesh size in million (M)	n^+_{mean}	Δs^+_{max}	Δl^+_{max}
Coarse	3.88	0.28	28	71
Medium	8.35	0.27	14	29
Fine	10.78	0.26	13.5	26

To further investigate the adequacy of the spatial resolution of the meshes, the time-averaged velocity profiles in the near wake are compared. Figs. 2 and 3 compare the velocity profiles in the wake of the GTS for $X/H \leq 2$ for the PANS - AVL SMART schemes and PANS - CDS, respectively. The flow topology when the AVL SMART schemes were used was anti-symmetric to those observed when CDS is used, and thus, the comparison between the flow states of similar topology is performed. Shown in Fig. 2(a) (3(a)) and 2(b) (3(b)) are streamwise and vertical velocity profiles at the specified locations in the near wake, respectively. In these plots, the x co-ordinate for the velocity profiles is obtained by the following relation: $X = x_o + ((u_{x,z}/U_\infty) - 1) \times 0.1$. Here, x_o is the x co-ordinate, u_x, and u_z are the values of mean streamwise and vertical velocities, respectively. The velocity profiles were measured at intervals of $0.25H$ from the base to $X/H = 2$. Three cases are chosen for PANS with AVL SMART schemes; medium mesh with ASR, medium mesh with ASB, and fine mesh with ASB. The velocity profiles of the medium and fine mesh are in good agreement in the near wake, although a very slight mismatch is observed near the saddle point region near $X/H \simeq 1$, indicating that the medium mesh can accurately replicate the flow features as the fine mesh, thereby, achieving the primary objective of using the PANS simulations - that accurate results can be obtained on coarser grids (Krajnović et al. (2012a)). It may be noted that the coarse mesh with 3.88 million elements does not accurately predict flow topology as seen in Fig. 4(a), and is not used in the comparison of the velocity profiles. It may be recalled that the velocity profiles and the location of vortex centres obtained from the LES on this grid showed good agreement with the results of the medium and fine mesh (see Fig. 5). A minimum threshold is thus required for the PANS equations to accurately predict the flow.

Fig. 3 compares the velocity profiles in the wake of the GTS when PANS with CDS is used, with the results from the fine mesh of LES from Rao et al. (2018b). It may be recalled that the flow topology in the vertical midplane in the LES of Rao et al. (2018b) is in flow state II, which is anti-symmetric to that observed in previous experimental studies. Using CDS with PANS results in flow state II, and the velocity profiles obtained here can be directly compared with those obtained from LES. The results of the medium and the fine mesh with PANS - CDS are compared with the results of the fine mesh from LES. As seen in Fig. 4, the recirculation region is elongated in the streamwise direction, with the saddle point located further away from the base. This results in a larger mismatch of the velocity profiles between the medium and the fine mesh using PANS - CDS, while the velocity profiles obtained from the fine mesh are closer to that obtained from an identical mesh using LES.

3. Results

3.1. $\beta = 0^\circ$

The flow topology in the near wake of the GTS model is investigated using the AVL SMART and central differencing schemes using the PANS

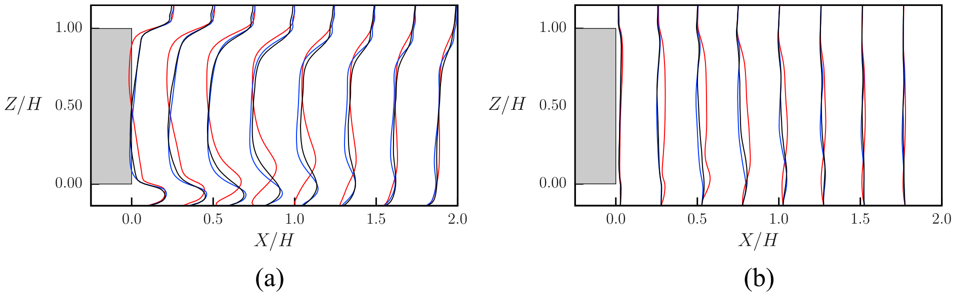

Fig. 3. (Colour online) Comparison of the velocity profiles in the wake of the GTS model in the vertical midplane when CDS is used. (a) streamwise velocity and (b) vertical velocity. The black, red and blue lines correspond to the fine mesh with LES, medium mesh with PANS - CDS, and fine mesh with PANS - CDS, respectively. Flow is from left to right in these images.

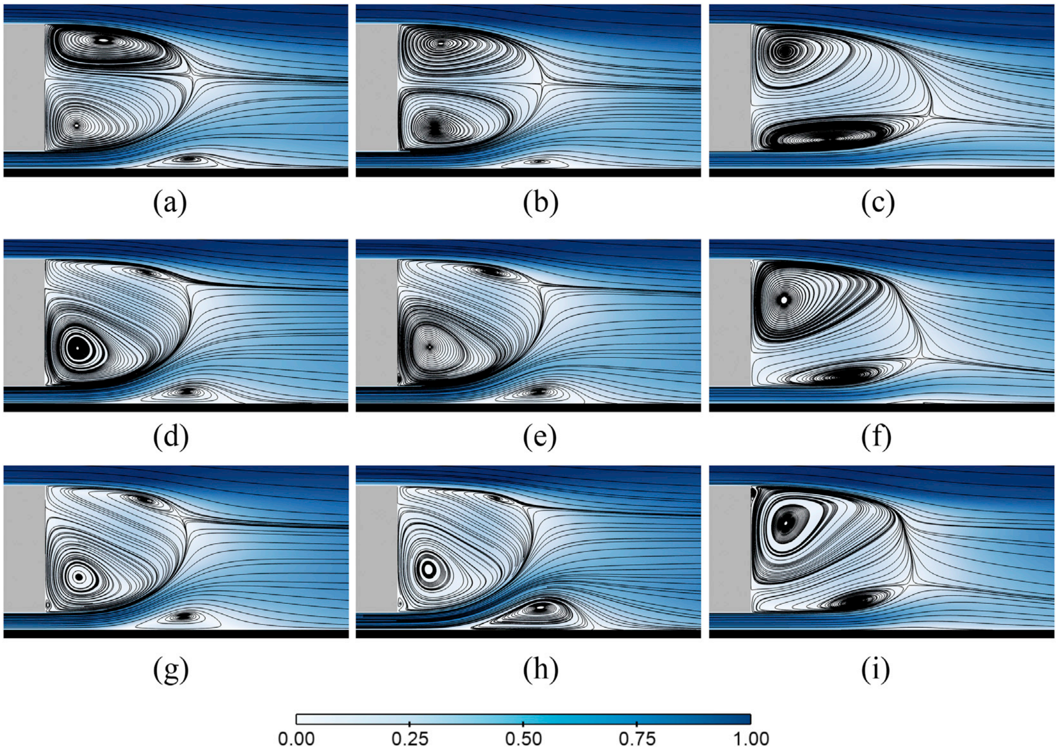

Fig. 4. (Colour online) Visualisation of the contours of the normalised time-averaged velocity overlaid with streamlines in the vertical midplane at the rear of the GTS at a gap height of $G/H = 0.14$ for the specified cases: Top row: coarse mesh; middle row: medium mesh; bottom row: fine mesh - (g) and (i), and polyhedral mesh - (h). Differencing scheme ASB is used in (a), (d), (g) and (h); ASR in (b) and (e); and CDS in (c), (f) and (i). Flow is from left to right in these images.

equations when the incoming flow is in-line to the longitudinal midplane. Shown in Fig. 4 are the contours of the time-averaged velocity overlaid with streamlines in the vertical midplane at the rear of the GTS. Three schemes are used: AVL SMART Bounded (ASB), AVL SMART Relaxed (ASR) and a blend of central differencing scheme - 95% and upwind scheme - 5% (CDS), on the three-meshes of increasing spatial resolution. While the coarse mesh fails to accurately predict the asymmetric flow topology for both the ASB and ASR schemes, using the CDS produces an anti-symmetric flow topology (similar to flow state II); although the tiny vortex adjacent to the large triangular vortex is not captured. The saddle point for ASB is above the lateral midplane, while it lies on the midplane for ASR. For the medium mesh, the flow topologies using ASB and ASR schemes for the momentum equations are identical, and the flow topology is similar to that observed in the experiments of McArthur et al. (2016) and the numerical simulations of Gunes (2010) - flow state I. However, when the PANS equations are used with CDS, the flow topology is anti-symmetric to the experiments - flow state II (Fig. 4(f)), but similar to the results of the LES of Rao et al. (2018b) and Ortega et al. (2004), and to the recent experimental investigations of Schmidt et al. (2018). As the spatial resolution is further increased, the flow topologies are similar to those observed on the medium mesh; although the smaller elliptical-shaped vortex in Fig. 4(i) is smaller as compared to its counterpart in Fig. 4(f). Also discernible in these images is the formation of a ground vortex below the saddle point when ASB and ASR are used (not evident in the experimental work of McArthur et al. (2016)), and the curvature of the bounding streamline (separatrix) for simulations with ASB and ASR is influenced by this ground vortex. As the computational costs using the fine mesh are higher as compared to the medium mesh, and given the good agreement between the velocity profiles in Fig. 2, the simulation with ASR on the fine mesh is not performed. A standalone simulation performed using a polyhedral mesh of approximately 5.5 million elements constructed using AVL FAME™M using ASB scheme also resulted in flow state I. However, the ground vortex observed in the simulations with the polyhedral mesh is significantly larger to those observed when hexahedral meshes are used. It may be recalled that a large ground vortex (approximately 0.3H in height) was observed at $G/H = 0.11$ in the experimental work of McArthur et al. (2016), and perhaps a slight change in the velocity prediction between the GTS and

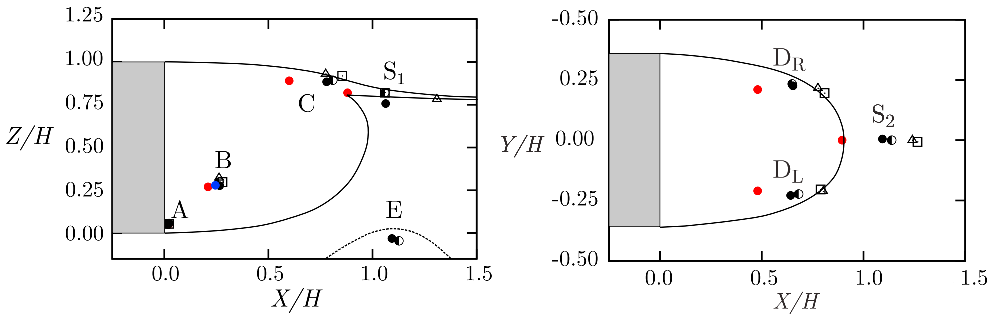

(a)

(b)

Fig. 5. (Colour online) Location of the centre of the vortices obtained from the time-averaged wake of the GTS in (a) the vertical midplane and (b) lateral midplane. While the flow topology in the simulations with CDS is anti-symmetrical to those observed in the experiments, the vortex locations are transposed to compare directly with previous experimental studies, and to those obtained from ASB scheme. For each vortex location and the saddle point, the medium mesh - ASB (◐), fine mesh - ASB (●), the medium mesh - CDS (△), fine mesh - CDS (□) are compared with the water channel experiments of McArthur et al. (2016) (●) at an identical Reynolds number, and to the wind tunnel experiments of Storms et al. (2001) (●) at $Re_W = 2 \times 10^6$. The bounding streamlines (separatrix) from McArthur et al. (2016) are marked by black continuous lines. The dashed black line represents the boundary of the ground vortex. Flow is from left to right in these images.

the ground may lead to the change in the size of this ground vortex (also see Castelain et al. (2018)). However, in flow state II, the ground vortex is suppressed as a result of the larger downwash as compared to flow state I. It may be noted that the polyhedral mesh had larger cell sizes at distances close to the boundaries of the computational domain, and this restricted the use of CDS/LES on this mesh. Furthermore, the number of internal cell faces for the polyhedral mesh was significantly higher compared to the hexahedral mesh of similar cell count, which resulted in longer run-times. Nonetheless, these simulations indicate that the flow topology in the first few flow passages is largely dependent on the numerical scheme used, as compared to the type of elements used for the construction of the computational domain (also see Pereira et al. (2015), Vaz et al. (2015)). The contours of the dynamic parameter in the PANS simulations (f_k) is shown in Appendix C.

Fig. 5(a) and (b) show the location of the centre of the vortices for the medium and fine meshes using the ASB and CDS in the vertical and lateral midplanes, respectively. In the vertical midplane, the location of the centre of the tiny vortex (A) adjacent to the large triangular vortex (B), and the upper vortex (C) are marked. In the lateral midplane, the two symmetric counter-rotating vortices that are observed are marked by D_R and D_L, indicating the left and right vortices. The saddle points in the vertical and lateral midplanes are marked S_1 and S_2, respectively. The bounding streamline, or the separatrix in both the planes is marked by continuous black lines. In Fig. 5(a), the centre of the ground vortex (E) observed for the PANS - ASB cases have been shown. The centres of these vortices lie directly beneath the saddle point in the flow. While the centres of the $D_{R,L}$ vortices, vortex C and the saddle points $S_{1,2}$ are located farther downstream as compared to that observed in the experimental investigations of McArthur et al. (2016), the centres of vortices A and B are closer for all the schemes tested. The location of the vortex centres for the medium and fine meshes for the simulations with ASB scheme are close to each other in both the planes (also confirming the good agreement in the match between the velocity profiles as seen in Fig. 2(a)). However, the location of the centre of the vortices are closer to the experimental results when ASB scheme is used as compared to that when CDS is used, although the vortex centres obtained from ASB scheme are $\simeq 20 - 25\%$ further downstream compared to the location of McArthur et al. (2016). Thus, using the CDS, not only results in an anti-symmetric flow topology, but also results in the location of the vortex centres being located further downstream.

Grandemange et al. (2013a) observed that the influence of the ground clearance is not significant for gap heights of $G/W \geq 0.1$, which indicates that the flow topology is largely dependent on the geometrical configuration of the body. Show in Fig. 6(a) and (b) are the contours of the time-averaged velocity for the GTS at $G/H = 1.1$ using ASB and CDS, respectively. While the ASB scheme produces a symmetric flow topology in the vertical midplane, the CDS produces an asymmetric flow topology similar to the LES results of Rao et al. (2018b) - flow state II, and to that at lower gap heights when CDS is used, but anti-symmetric to that observed in the experiments. The location of the centres of the vortices for the PANS - CDS case was nearly identical to that observed in the LES of Rao et al. (2018b), providing further confidence in the meshes used for this study. It may be recalled that a symmetric flow topology had previously been observed when the flow is averaged over the two flow states (Volpe et al. (2014a), Volpe et al. (2015)). To ensure that the mean velocity contours shown for the ASB scheme in Fig. 6(a) is not the resultant of averaging over the two flow states, the forces and the flow fields are checked at different instants in time, and a symmetric flow topology is observed over the course of the simulation. More recently, a transient-symmetric state (TS) has been identified in the wake of a squareback bluff bodies (Varon et al. (2017), Kaiser et al. (2014), Vidales (2016), (Pavia et al. (2017)), which is an intermediate symmetric flow state observed during the switching process for short durations between the two stable flow states. While the probability of the TS state to be the first flow state observed in the GTS wake is rather low; longer simulation times are required to investigate if the symmetric flow state observed with PANS - ASB, would further evolve into either of the two possible reflection-symmetry breaking states. Standalone simulations performed using the RANS two-equation $k - \varepsilon$ turbulence model showed a weak asymmetry in the vertical midplane at this gap height (see Fig. 15(b) in Appendix B).

Upon examining the contours of the unresolved kinetic energy (see Appendix C), the values of the unresolved kinetic energy are two orders of magnitude lower for the GTS at $G/H = 1.1$ as compared to $G/H = 0.14$ (and to the total kinetic energy), thereby leading to very low values of f_k in the near wake. In such cases, the modelling of the small unresolved scales will not significantly impact the overall solution, and the numerical errors would mainly contribute to the overall accuracy (Basara et al. (2018), Krajnović et al. (2016), Park et al. (2004)). More recently, Pereira et al. (2018b) observed that the dependence on the spatial and temporal resolution is larger when $f_k \to 0$. For the GTS at $G/H = 1.1$, the spatial and temporal requirements are satisfied by the use of LES-capable grids and very low time-step (the non-dimensionalised time-step for the current simulations is $\simeq 0.002$), respectively. The differencing scheme plays a larger role in such cases; and CDS is more accurate (and less dissipative) as compared to the AVL SMART schemes (also see Trias et al. (2014), Verstappen and Veldman (2003)), resulting in a flow state similar to the LES when PANS - CDS is used (flow state II). While the flow topology cannot be predicted *a priori*, the influence of the differencing schemes needs to be investigated for bluff body flows where bi-stable flow is

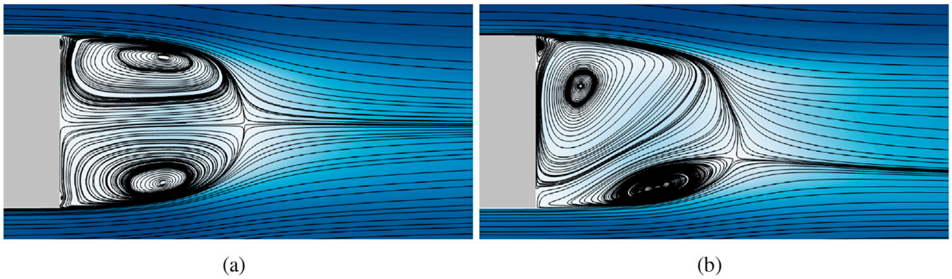

Fig. 6. (Colour online) Visualisation of the contours of the normalised time-averaged velocity overlaid with streamlines in the vertical midplane at the rear of the GTS at a gap height of $G/H = 1.1$ for (a) ASB scheme and (b) CDS. Contour shading as per Fig. 4. Note that the resolution of this mesh is similar to that of the medium mesh. Flow is from left to right in these images.

probable or when the unresolved kinetic energy is very low. Lately, attempts made to incorporate blending of the AVL SMART scheme with CDS based on the value of the dynamic resolution parameter in PANS (f_k) for a square-shaped cylinder at $Re = 2.2 \times 10^4$ showed promising results as compared to using LES, or PANS with pure CDS and/or AVL SMART schemes (see Basara et al. (2018)). The use of such scheme combinations, and the use of CDS when f_k decreases below a pre-set threshold ($f_k \simeq 0.2 - 0.4$) could further aid in improving the flow prediction in PANS simulations.

In all these simulations, the (initial) flow topology predicted by using CDS (including the LES of Rao et al. (2018b), where central differencing scheme is used) remains invariant (flow state II), albeit the minor changes in the velocity profiles and the location of the centre of the vortices; while using AVL SMART schemes results in a flow topology similar to the experimental works for the GTS near the ground (flow state I), but not at large gap heights. It must be reiterated that the run-times for these cases involved only a few flow passages through the domain, and this does not allow for the exploration of the switching behaviour between the two flow states when each of the two schemes are used exclusively.

Fig. 7 shows the distribution of the (normalised) Reynolds normal stresses in the three directions for the PANS - ASB. With flow topology in the vertical midplane being similar to that observed in previous experimental works, the distribution of the Reynolds stresses in the lateral and vertical midplanes are similar to those observed in McArthur et al. (2016). While the maximum stresses occur in the streamwise direction in the vertical midplane (see Fig. 7(a)), the distribution of the streamwise stresses in the vicinity of the ground vortex are also observed, and the intensity is larger than that observed in the experiments. Note that the contour levels are similar to that used in McArthur et al. (2016). Furthermore, in the lateral midplane, the distribution of the stresses in the streamwise direction is on the outer periphery of two counter rotating vortices. The Reynolds stresses in the other two directions are concentrated in the region of the saddle point, in both the vertical and lateral midplanes. The distribution of the stresses in the vertical midplane for the PANS - CDS is similar to that observed in the LES of Rao et al. (2018b) (not shown).

The isosurfaces of the Reynolds normal stresses in the near wake are shown in Fig. 8 for the PANS simulations with ASB scheme. Consistent with the distributions seen in Fig. 7, the streamwise stresses are stronger in the upper shear layer associated with the smaller vortex, and along the sides parallel to the longer edges of the GTS, while it is lower in the region associated with the larger triangular vortex. Furthermore, the distribution of the stresses around the ground vortex is also seen in Fig. 8(a), which extends to a width approximately equal to that of the GTS in the lateral direction. The distribution of the stresses in the other two directions is concentrated within the confines of the $\langle u'^2_x \rangle$, with the distribution of $\langle u'^2_y \rangle$ extending further downstream as compared to $\langle u'^2_z \rangle$. Although the stress intensities are slightly lower than that observed in the LES of Rao et al. (2018b), they compare well with the distributions observed in McArthur et al. (2016).

The pressure distribution on the base is shown for the two different flow states observed using PANS - ASB and PANS - CDS. Fig. 9(a) and (b) show the contours of the pressure coefficient ($C_p = 2(p - p_\infty)/\rho U^2_\infty$) on

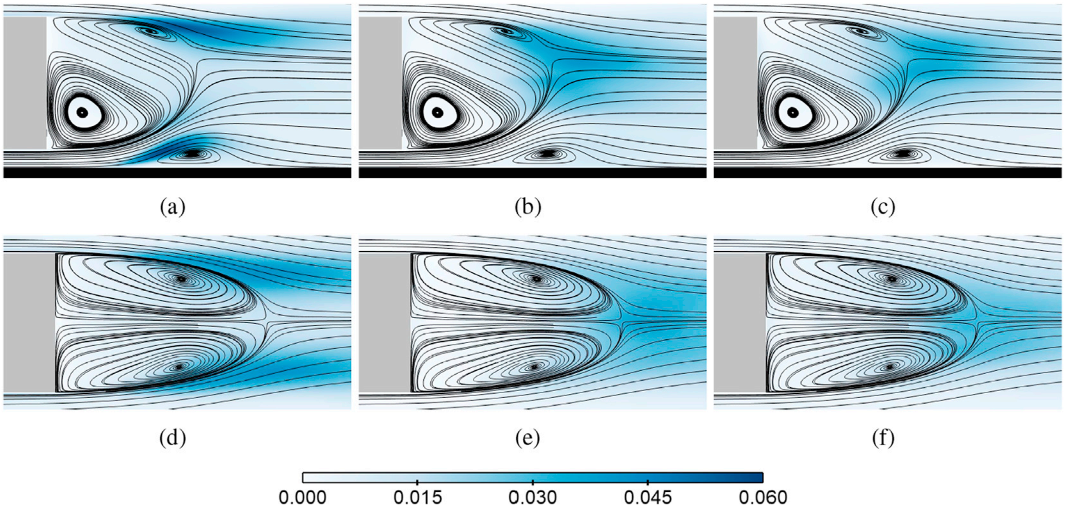

Fig. 7. (Colour online) Visualisation of the contours of the Reynolds normal stresses obtained using the PANS - ASB scheme at the rear of the GTS model overlaid by streamlines in the vertical midplane (a)–(c), and in the lateral midplane (d)–(f). $\langle u'^2_x \rangle$ - (a) and (d), $\langle u'^2_y \rangle$ - (b) and (e), and $\langle u'^2_z \rangle$ - (c) and (f). Flow is from left to right in these images.

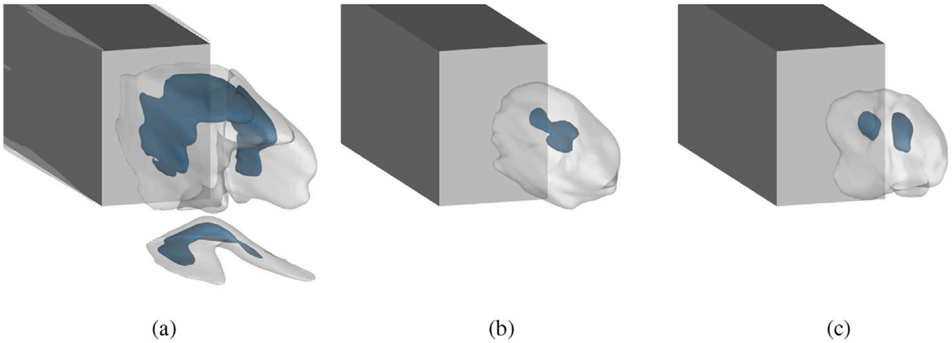

Fig. 8. (Colour online) Distribution of the Reynolds normal stresses obtained using the PANS - ASB scheme behind the GTS model for the incoming flow at $\beta = 0°$. (a) $\langle u'^2_x \rangle$, (b) $\langle u'^2_y \rangle$ and (c) $\langle u'^2_z \rangle$. Isosurface levels: blue: 0.02, white: 0.0375. Flow is from top left to bottom right in these images.

the base for PANS - ASB and PANS - CDS, respectively for the fine mesh of the GTS at $G/H = 0.14$. Here, p and p_∞ are the local and the reference pressures, respectively, and ρ is the density of air ($= 1.1885\ \mathrm{kgm}^{-3}$). The contours between the two cases are transposed across the lateral midplane, further indicating that the change in the flow state when two different schemes are used. The proximity of the vortex centre of the large triangular vortex is responsible for the region of lower pressure, which occurs below the lateral midplane for the PANS - ASB, and above for PANS - CDS, as seen in Fig. 10. These images are analogous to the pressure coefficient on the base of the squareback Ahmed body (Lucas et al. (2017), Eulalie et al. (2017)), when conditionally-averaged over one flow state. While the pressure coefficient is symmetrical about the lateral midplane for the squareback Ahmed body, they are symmetrical about the vertical midplane for the GTS (also see McArthur et al. (2018)). Fig. 9(c) and (d) show the contours of the pressure coefficient on the base for PANS - ASB and PANS - CDS for the GTS at $G/H = 1.1$. As a result of the symmetrical flow topology observed in the wake when the ASB scheme is used, the pressure distribution remains nearly constant across the base as seen in Fig. 9(c). Asymmetrical flow topology is observed when CDS is used (Fig. 9(d)), resulting in a flow topology similar to that observed in the LES of Rao et al. (2018b) (flow state II), and to that seen at low gap heights when PANS - CDS is used. Although the flow state using CDS remains invariant with gap height and results in flow structures that are topologically similar; the differences between the pressure distributions across the base can be observed between Fig. 9(b) and (d), with the high-pressure region located higher along the base at $G/H = 0.14$ as compared to $G/H = 1.1$.

Fig. 10(a) and (b) show the pressure coefficient torus behind the GTS at $G/H = 0.14$ in the two flow states observed in the PANS simulations using ASB and CDS, respectively. The formation of a slanted C_p torus has previously been reported in the wake of a squareback Ahmed body (Krajnović and Davidson (2003), Volpe et al. (2015), Grandemange et al. (2013b), Volpe et al. (2014b), Lucas et al. (2017), Barros et al. (2017a), Eulalie et al. (2017) and others) when conditionally averaged over one flow state. Bi-stability or the switching phenomenon has not been observed in the simulations when started from a quiescent condition, thereby leading to the formation of a torus which is slanted in the streamwise direction indicating the occurrence/dominance of only one flow state for the chosen numerical scheme. The C_p torus closely contours the vortex cores (indicated by red lines) which are obtained from the time-averaged velocities. As seen in these figures, the vortex cores are closer to the base at the bottom and top for ASB and CDS, respectively. Also discernible in Fig. 10(a) is the presence of the ground vortex, which spans approximately 50% of the width of the base. Fig. 10(c) and (d) show the isosurfaces of C_p when the GTS model is placed above the ground plane at $G/H = 1.1$ for the PANS simulations using ASB and CDS, respectively. A symmetrical flow topology is observed when the ASB scheme is used, resulting in the C_p torus (and vortex cores) being parallel to the base of the model, while a slanted torus is observed when CDS is used.

In order to observe the coherent structures in the two flow states, the isosurfaces of the time-averaged helicity ($\mathscr{H}$) are visualised in Fig. 11. Helicity is a vortex identification method, and is defined as the scalar product of the velocity and the vorticity (also see Levy et al. (1990),

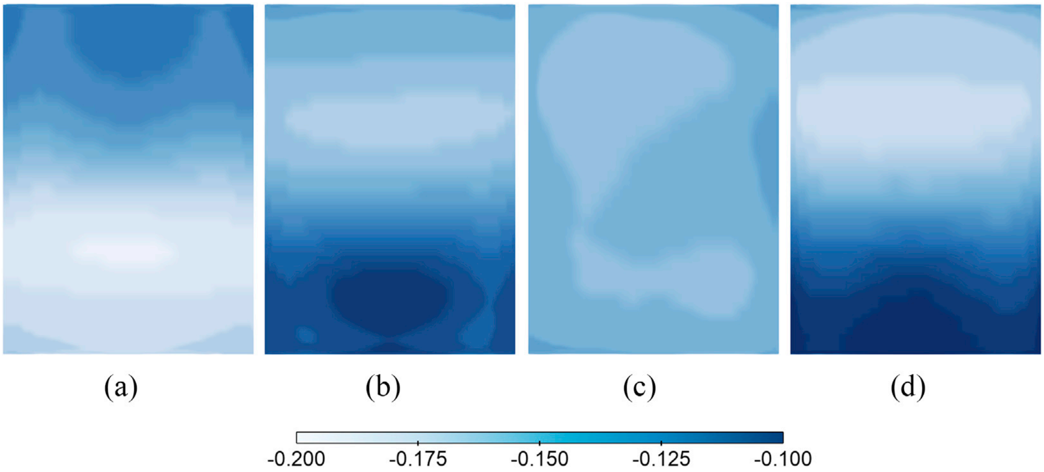

Fig. 9. (Colour online) Visualisation of the contours of the pressure coefficient on the base of the GTS model at $G/H = 0.14$ for (a) PANS - ASB, (b) PANS - CDS; and at $G/H = 1.1$ for (c) PANS - ASB, and (b) PANS - CDS.

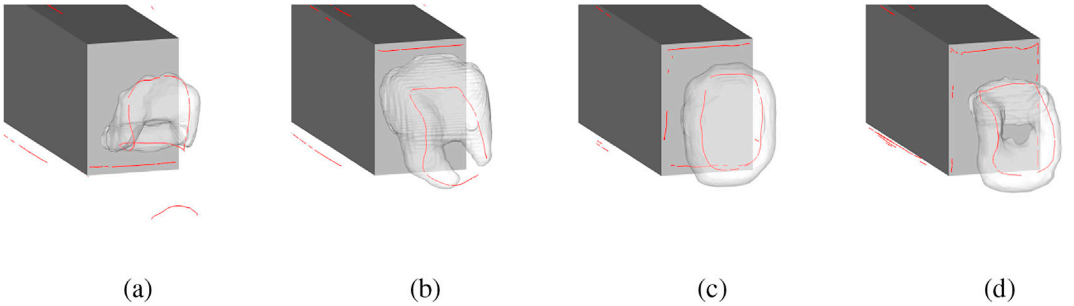

Fig. 10. (Colour online) Visualisation of the translucent isosurfaces of the pressure coefficient behind the GTS model at $G/H = 0.14$ for (a) PANS - ASB, $C_p = -0.215$ and (b) PANS - CDS, $C_p = -0.17$; at $G/H = 1.1$ for (c) PANS - ASB, $C_p = -0.2$ and (b) PANS - CDS, $C_p = -0.2$. Flow is from top left to bottom right in these images.

Moffatt and Tsinober (1992), Moffatt (1969), Hunt and Hussain (1991)). Helicity has previously been used to identify streamwise vortex structures in turbomachinery, magneto-hydrodynamics and in the wake of bluff body flows (e.x., Engels et al. (2018), Yamada and Miyata (1993)). Fig. 11(b) and (c) show the isosurfaces of helicity coloured by the time-averaged velocity for flow state I obtained from the PANS - ASB scheme, where the large triangular-shaped vortex in the mean flow occurs closer to the ground (see Fig. 11(a)), while Fig. 11(e) and (f) show the anti-symmetric flow state (flow state II) obtained from the LES of Rao et al. (2018b) (see Fig. 11(d)).

The formation of the two counter-rotating vortices is observed and extends downstream beyond the near wake (and recirculation region) of the GTS, and the vortices are observed marginally below the lateral midplane in PANS - ASB simulation, while they are observed marginally above it in the LES. Fig. 11(e) and (f) compare well with those observed in Ortega et al. (2004), where a truncated GTS model was used for their numerical analysis at $Re_W = 2 \times 10^6$. Nonetheless, these images validate the schematic of the flow topology shown Evrard et al. (2016), Perry et al. (2016) and Schmidt et al. (2018) for the two reflectional symmetry breaking flow states. It may be noted that when the squareback Ahmed body was considered, the pair of counter rotating vortices were symmetrical about the lateral midplane, and in the case of the GTS/GETS, it is symmetrical about the vertical midplane. Also visible in Fig. 11(b) and (e) are the corner vortices which originate at the front of the model; with the bottom corner vortices extending further downstream as compared to the ones at the top.

3.2. Switching between the flow states

In the simulations performed so far, switching between the two flow states was not observed, and the flow states were fixed to their respective configuration over the duration of simulations. It may be recalled that flow state I was observed when ASB was used, while CDS resulted in flow state II. In order to investigate if a differencing scheme used for the convective terms results in a particular flow topology, the saved solution from the PANS - ASB simulation obtained using the fine mesh (consisting of 10.78 million elements) was restarted with the CDS. Shown in Fig. 12(a) and (b) are the time-histories of the drag and lift force coefficient for the GTS model at $G/H = 0.14$. After seven flow passes through the domain ($t = 106.4$s), the numerical scheme was changed to CDS. This resulted in a decrease of the drag coefficient, while an increase in the lift force coefficient was observed. This change in the forces is accompanied by a change in the flow topology from flow state I to flow state II, as shown in Fig. 12(c) – 12(h), where the instantaneous velocity contours in the vertical midplane are visualised from the instant of switching at $t = 106.4$s, to a later time instant of $t = 144.4$s at every half-flow passage intervals (7.6s). At $t = 114$s (Fig. 12(d)), the distribution of the vortices is nearly symmetrical across the lateral midplane, although the location of the vortex centres are closer to those observed at $t = 106.4$s. This flow topology can perhaps be alluded to the unstable TS state described in Varon et al. (2017), Vidales (2016) and Kaiser et al. (2014). At a later time instant of $t = 121.6$s (Fig. 12(e)), a larger vortex forms above the lateral midplane, with smaller vortices being observed closer to the

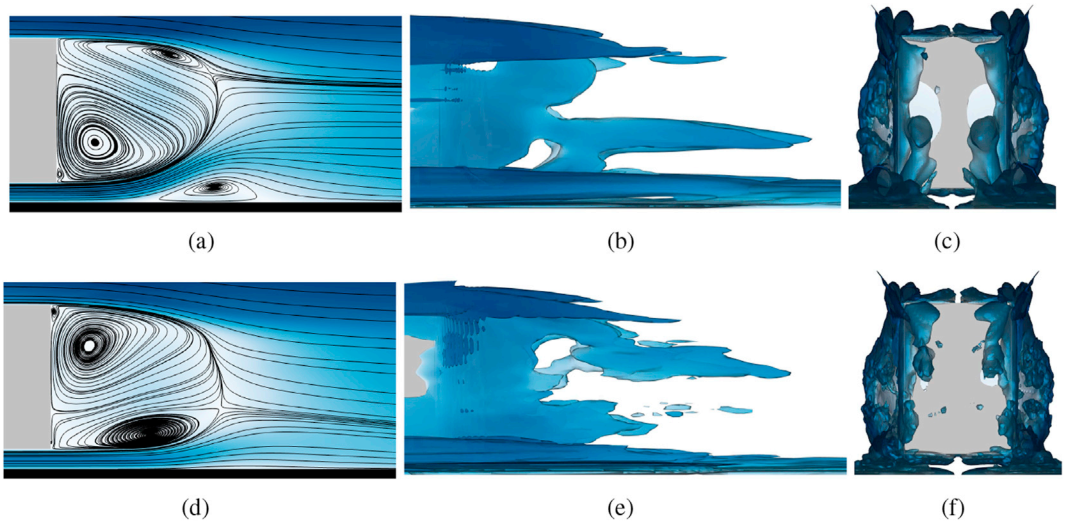

Fig. 11. (Colour online) Visualisation of the time-averaged velocity in the vertical midplane (PANS - ASB - (a) and LES - (d)) and the translucent isosurfaces of time-averaged helicity ($\mathscr{H} = 1.25$ ms^{-2}) coloured by the normalised time-averaged velocity for the fine meshes using PANS - ASB - (b) and (c), and LES - (e) and (f). Subfigures (a), (b), (d) and (e) are in left side view, while (c) and (f) are captured from a point directly behind the base and looking upstream. Contour shading as per Fig. 4. Flow is from left to right in (a), (b), (d) and (e).

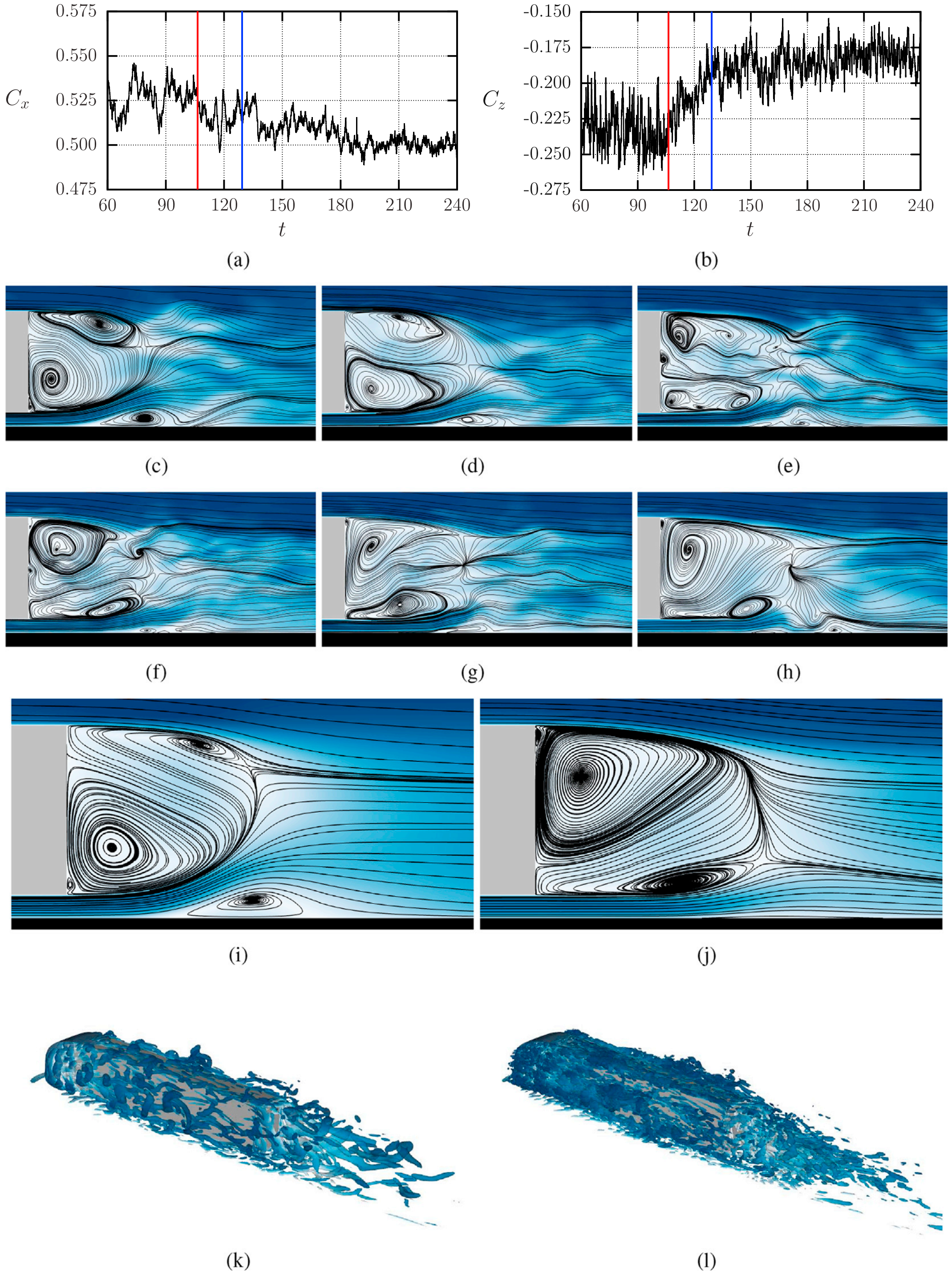

Fig. 12. (Colour online) Time-histories of the drag coefficient (a), and lift force coefficient (b) for the GTS model at $G/H = 0.14$ for the PANS simulation on the fine mesh. The vertical red line at $t = 106.4$s indicates the time-instant when the differencing scheme was changed from ASB to CDS. Visualisation of the (normalised) instantaneous velocity contours overlaid with streamlines at time intervals of 7.6s at time-instants of (c) $t = 106.4$s, (d) $t = 114$s, (e) $t = 121.6$s, (f) $t = 129.2$s (the start time of averaging indicted by the vertical blue line), (g) $t = 136.8$s and (h) $t = 144.4$s. Visualisation of the (normalised) time-averaged velocity contours overlaid with streamlines at the end of each averaging period, showing flow state I for $15.2\,\mathrm{s} \le t \le 106.4$s (i), and flow state II for $129.2\,\mathrm{s} \le t \le 243.2$s (j). Visualisation of the translucent isosurfaces of Q-criterion ($Q = 15s^{-2}$) coloured by the normalised velocity for ASB scheme at (k) $t = 106.4$s, and after switching to CDS at (l) $t = 129.2$s. Contour shading as per Fig. 4. Flow is from left to right in images (c)–(l).

ground, and at $t = 129.2$s (Fig. 12(f)), the flow topology is reminiscent of flow state II observed when the PANS simulations are started with CDS. The height of the ground vortex diminishes as the flow topology switches from flow state I to flow state II, and this flow state is retained at later time-instants of $t = 136.8$s (Fig. 12(g)) and $t = 144.4$s (Fig. 12(h)), and until the end of the simulation at $t = 243.2$s. It may also be noted that the location of the centre of the large triangular vortex in the instantaneous snapshots in Fig. 12(f) – 12(h) does not vary as much as the centre of the smaller elliptical shaped vortex, which is consistent with the observations of McArthur et al. (2016) and Lo and Kontis (2017).

The mean flow topology in the vertical midplane obtained from conditional averaging of flow states I and II are shown in Fig. 12(i) and (j), respectively. Here, flow state I is averaged after the first flow passage from $t = 15.2$s to $t = 106.4$s, while flow state II is averaged from $t = 129.2$s to $t = 243.2$s. The snapshots of the instantaneous flow contours capture the predominant vortex structures observed in the mean flow topology, with the location of the vortex centres close to that observed in the mean flow. Fig. 12(k) and (l) show the isosurfaces of Q-criteria (Jeong and Hussain (1995)) when ASB and CDS are used, respectively. Hairpin loop-type structures are observed when ASB scheme is used; while finer-scale/thin elongated structures are observed when CDS is used (also see section 3 of Basara et al. (2011)).

When the differencing scheme was changed from CDS to ASB scheme for the PANS simulation based on the fine mesh, a similar switching behaviour to the one previously described is observed, with the flow topology switching from state II to state I. The switch is accompanied by an increase in the drag coefficient and a decrease in the lift coefficient as the flow transitions from state II topology to state I topology as seen in Fig. 13(a) and (b), respectively. The onset of the switching process occurred nearly three through-flows after the scheme was changed from CDS at $t = 108$s as compared to the case where the scheme was changed from ASB to CDS, where the switching process occurred shortly after the change in the scheme. In order to check if this transition would have occurred without the change in the differencing scheme, the PANS - CDS simulation was integrated beyond $t = 160$s (as indicated by the gray lines in the time-history plots). The flow retained its state II topology, indicating that the change in the numerical scheme indeed triggers the transition. Fig. 13(c) to 13(n) show the normalised instantaneous velocity contours at various stages of the transition from state II to state I in the vertical midplane of the GTS in the near wake. At $t = 159.6$s (Fig. 13(c)), a flow topology reminiscent of the flow state II topology is observed, prior to an increase in the drag force coefficient. The flow then goes through a reorganisation of the vortices (Fig. 13(d) and (e)), where a near-symmetrical flow topology is observed - the transient-symmetric state, with the centres of the two vortices being equidistant to the base of the GTS. At $t = 182.4$s (Fig. 13(f)), a flow topology resembling state I is observed. However, this flow state is not retained with the flow reverting back to the TS state over the next two through-flow periods, as seen in Fig. 13(g) – 13(k). This change is accompanied by a sudden decrease in the drag coefficient and a marginal increase in the lift coefficient as seen in the force histories around $t = 190$s. The unstable TS state appears to temporarily revert back to a state II topology (see Varon et al. (2017)), but this transition to the original flow topology does not occur. While the TS state lasted for a short period when the flow switched from state I to state II, a relatively longer period of the TS state is observed here. It may be noted that Varon et al. (2017) classified this as the “third” flow state, indicating tri-modality of the flow behaviour. At $t = 220.8$s, flow state I topology is observed (Fig. 13(l)); which is retained at later time instants of $t = 258.4$s (Fig. 13(m)) and $t = 281.2$s (Fig. 13(n)); although a decrease in the drag force coefficient occurs around $t = 260$s, the flow does not revert back to state II topology. The mean drag and lift coefficient evaluated after the switching event for both the cases are within 1% of that obtained from the PANS simulations where ASB or CDS were used exclusively (see Table 2).

A similar switching behaviour is observed for the GTS at a gap height of $G/H = 1.1$. When the differencing scheme is changed from ASB to CDS, the flow transitions from a symmetric flow topology in the vertical midplane to a flow state II topology; while a change in the scheme from CDS to ASB leads to the formation of a pair of symmetrical vortices in both the vertical and lateral midplanes.

The switching behaviour is a physical phenomenon which occurs at random intervals, and run-times of the order of hundreds of seconds are required to observe such behaviour experimentally (Grandemange et al. (2013b), Cadot et al. (2015) Schmidt et al. (2018)); here, switching between the two flow states was artificially triggered by a change in the differencing scheme as opposed to that observed naturally in the wake of a simplified truck model and a squareback Ahmed body (Dalla Longa et al. (2017)). It may be recalled that switching between the flow states was not reported in the water-channel experiments of McArthur et al. (2016), with flow state I being observed over the duration of the experiments, and perhaps being “locked” into this configuration due to the streamlined support structures underneath the body. A small asymmetry introduced by yawing the incoming flow by 2.5° also failed to trigger a change in the flow state in the LES of Rao et al. (2018b). It could be speculated that small changes in the velocity field in the near wake could lead to the vortices being reorganised to their stable individual configurations observed when each scheme was used exclusively. (Note that the fine mesh was used in both cases to minimise the discretisation errors). Recent DNS of a two-dimensional square-shaped Rayleigh-Bénard cell showed that small-scale intermittency (or noise) corresponding to the fraction of energy in unresolved scales was capable of triggering large-scale destabilisation events in reflectional symmetry breaking flows (see Podvin and Sergent (2017), Podvin and Sergent (2015), Trias et al. (2014), Östh et al. (2014) and references therein). A change in the numerical scheme perhaps produces white/numerical noise of sufficiently high amplitude, thereby triggering the transition from one flow state to the other in the wake of the GTS, in a manner similar to that observed in the flow reversal event in the two-dimensional Rayleigh-Bénard cell.

3.3. *Variation of the force coefficients*

Table 2 shows the variation in the time-averaged force coefficients for all the cases investigated in this study, along with those obtained from LES of Rao et al. (2018b). Flow state I and II indicate that the large triangular-shaped vortex is at the bottom and top in the time-averaged flows in the vertical midplane, respectively. The drag coefficient on the medium mesh using PANS is within 2% of that observed on the fine mesh for both flow states. The mean drag forces obtained from the PANS simulations are lower than their corresponding counterparts from LES, with those from PANS - CDS being marginally lower than PANS - ASB. The drag coefficient obtained from the PANS - ASB simulation on the polyhedral mesh is higher as compared to that observed on the hexahedral meshes, and results in flow state I topology. The two flow states are rather distinct when the incoming flow is at $\beta = 0°$, and can be identified based on the flow topology and pressure distribution across the base. The lift coefficient in the PANS simulations does not seem to vary significantly between the two flow states, as an averaged lift coefficient around $\langle C_z \rangle = -0.2$ is observed for the GTS at $G/H = 0.14$; while at larger gap heights, this value is close to zero.

4. Summary and conclusions

The flow past a simplified heavy vehicle - the GTS model is investigated at $Re = 2.7 \times 10^4$ using the PANS equations. With the asymmetric topology in the vertical midplane of the GTS susceptible to bi-stability, influence of the differencing scheme used for the convective flux on the prediction of the flow states is investigated here. Three differencing schemes are used: AVL SMART Bounded (ASB), AVL SMART Relaxed (ASR), and the central differencing scheme (CDS). The flow topology observed when ASB/ASR scheme is used was similar to that observed in the experimental work of McArthur et al. (2016) - flow state I, while using the CDS, the flow topology is anti-symmetric to flow state I, and is similar to that observed in the LES of Ortega et al. (2004) and Rao et al. (2018b) - flow state II. The time-averaged near wake is elongated in the streamwise direction when CDS is used, as compared to the results from PANS - ASB/ASR, with the location of the vortex centres and saddle points located further downstream. A higher spatial resolution is required when CDS is used with PANS to obtain a flow topology (and velocity profiles) closer to that of the LES, despite the mean drag coefficient computed being similar. The distribution of the Reynolds normal stresses obtained from the PANS - ASB on the hexahedral meshes were in

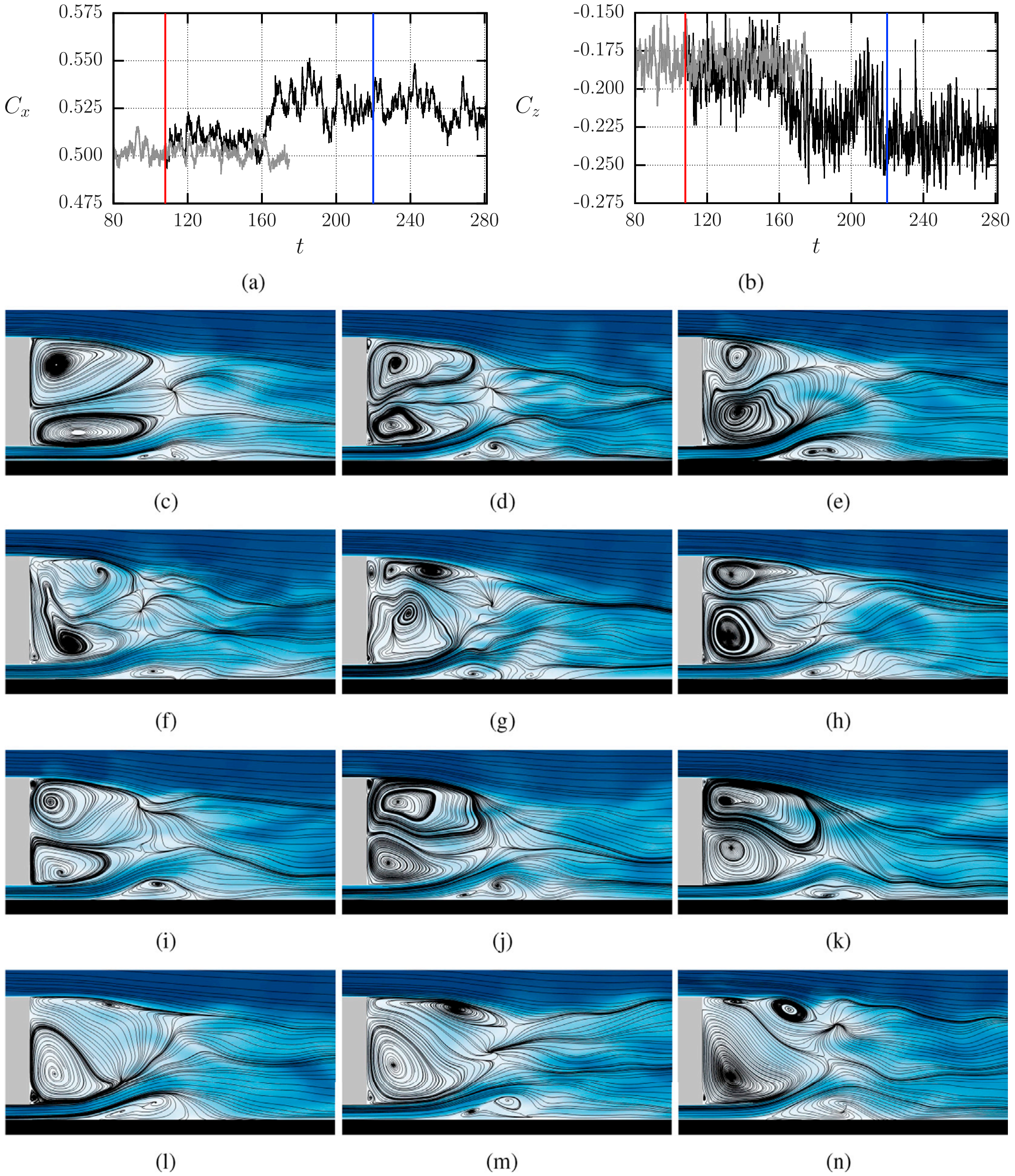

(a) (b)

(c) (d) (e)

(f) (g) (h)

(i) (j) (k)

(l) (m) (n)

Fig. 13. (Colour online) Time-histories of the drag coefficient (a), and lift force coefficient (b) for the GTS model at $G/H = 0.14$ for the PANS simulation on the fine mesh. The vertical red line at $t = 108$s indicates the time-instant when the differencing scheme was changed from CDS to ASB. The black line indicates the time-history of the forces when the differencing scheme is changed from CDS to ASB, while the gray line indicates the time-history of the forces when the PANS with CDS is used. Visualisation of the (normalised) instantaneous velocity contours overlaid with streamlines at time intervals of (c) $t = 159.6$s, (d) $t = 167.2$s, (e) $t = 174.8$s, (f) $t = 182.4$s, (g) $t = 190$s and (h) $t = 197.6$s, (i) $t = 205.2$s, (j) $t = 210.2$s, (k) $t = 212.8$s, (l) $t = 220.4$s (the start time of averaging indicted by the vertical blue line), (m) $t = 258.4$s, and (n) $t = 281.2$s. Contour shading as per Fig. 4. Flow is from left to right in images (c)–(n).

good agreement with those observed in McArthur et al. (2016), although higher distribution of the Reynolds stresses were observed in the vicinity of the ground vortex. The influence of the mesh construction on the flow topology was investigated by using a polyhedral mesh with the PANS - ASB scheme, in addition to the three meshes consisting of purely hexahedral elements. The flow topology obtained with the polyhedral mesh was similar to flow state I, although the ground vortex was slightly larger, and the recirculation zone elongated in the streamwise direction as compared to that observed on the hexahedral meshes.

Previous experimental investigations have shown that the flow topology in the vertical midplane of the GTS (or a parallelepiped bluff body) is invariant of the gap height for $G/H \geq 0.14$ (McArthur et al. (2016), Grandemange et al. (2013a)). When the GTS model was placed above the ground at $G = 1.1H$, flow state II was observed when PANS - CDS was used; while PANS - ASB showed a pair of symmetrical vortices in both the lateral and vertical midplanes at this gap height, and thus fails to accurately predict the asymmetrical flow topology observed behind the GTS. Very low values of the dynamic parameter - f_k are observed for both these cases, resulting in insufficient turbulence modelling as the unresolved kinetic energy is very low (Krajnović et al. (2016)). In such cases, the influence of the numerical scheme plays a larger role (see Pereira et al. (2018b)), and CDS accurately predicts the flow asymmetry in the vertical midplane.

The simulations performed here show that the differencing schemes used for the convective terms of the PANS equations play an important role in determining the near-wake flow topology of a squareback bluff

Table 2

Comparison of the time-averaged force coefficients and flow states observed in the wake of a simplified GTS model for the various cases undertaken in this study. * indicates polyhedral mesh. The root-mean-square (RMS) - $C_{y\ RMS}$ values are shown for the side force coefficients. † and ‡ indicate the value of the force coefficients computed after the numerical scheme was changed in PANS simulations. Unless otherwise stated, the gap height between the GTS and the ground plane is set to $0.14H$. Results from LES of Rao et al. (2018b) have also been shown for comparison.

Description	Mesh size (M)	$\langle C_x \rangle$	$C_{y\ RMS}$	$\langle C_z \rangle$	Flow state
LES	3.88	0.5724	0.0121	−0.1885	II
LES	8.35	0.5734	0.0123	−0.2010	II
LES	10.78	0.5608	0.0119	−0.1974	II
PANS - ASB	3.88	0.5091	0.0217	−0.2120	I
PANS - ASB	8.35	0.5196	0.0155	−0.2325	I
PANS - ASB	10.78	0.5294	0.0159	−0.2319	I
PANS - ASB *	5.5	0.5505	0.0158	−0.2147	I
PANS - ASR	3.88	0.5092	0.0184	−0.2059	I
PANS - ASR	8.35	0.5212	0.0161	−0.2330	I
PANS - CDS	3.88	0.4937	0.0098	−0.1971	II
PANS - CDS	8.35	0.5076	0.0088	−0.1920	II
PANS - CDS	10.78	0.5035	0.0111	−0.1837	II
PANS - ASB → CDS †	10.78	0.5037	0.0111	−0.1840	I→TS→II
PANS - CDS → ASB ‡	10.78	0.5254	0.0151	−0.2322	II→TS→I
$G/H = 1.1$ - LES	9.18	0.5776	0.0106	−0.0588	II
$G/H = 1.1$ - PANS - ASB	9.18	0.5402	0.0179	−0.0791	–
$G/H = 1.1$ - PANS - CDS	9.18	0.5250	0.0103	−0.0595	II

body. When AVL SMART schemes are used, the flow topology and the velocity profiles obtained from the medium mesh are in good agreement with those obtained from the fine mesh, and the flow topology is similar to that observed in previous experimental studies (flow state I). Central differencing schemes in PANS simulations generally require a higher spatial resolution for accurate solutions, and an anti-symmetric flow topology is observed in the near wake for the GTS (flow state II) when CDS is used. It may be noted that bi-stability or the switching between the two flow states was not observed in the numerical simulations when either ASB or CDS was used exclusively, due to the relatively shorter run-times as compared to experiments. However, when the differencing scheme was changed from ASB (CDS) to CDS (ASB), the flow transitioned from state I (II) to state II (I) with an intermediate transient-symmetric (TS) state (see Varon et al. (2017)), where the vortices in the near wake are temporarily symmetrical about the lateral midplane. In general, AVL SMART schemes can be used on meshes where the grid spacing is larger than that required for CDS, as in the case of the unstructured grid used here. Thus, using PANS with AVL SMART schemes is an alternative to using PANS - CDS/LES, where accurate solutions can be obtained on meshes of lower resolution. This study also highlights the importance of testing different numerical schemes for geometric configurations particularly sensitive to bi-stable flow, and such practices could become an integral part of computational fluid flow analysis using hybrid turbulence models/PANS simulations.

Acknowledgements

The authors would like to thank the computational support provided by Chalmers Centre for Computational Science and Engineering (C3SE) and National Supercomputer Centre (NSC), Linköping University provided by the Swedish National Infrastructure for Computing (SNIC). The authors would also like to acknowledge the support and licences provided by AVL GmbH, Austria. J. Z. also acknowledges the financial support from the Area of Advance Energy at Chalmers University of Technology and the Swedish Energy Agency under grant no. 43198-1.

Appendix A. Details of the polyhedral mesh

In addition to the hexahedral meshes, a polyhedral mesh was also used to investigate the flow topology using PANS - ASB, apart from the three hexahedral meshes for the GTS at $G/H = 0.14$. The polyhedral mesh was constructed in AVL FAME™M automatic meshing program. The CAD model of the GTS inclusive of the computational domain was first imported as stereolithography (.stl) file into the program and the boundary conditions were assigned. The near-wake region consists of three cylindrical refinement zones of increasing cell sizes, to accurately capture the flow. The program first creates a surface mesh, then builds the boundary layer around the body. This is followed by the formation of tetrahedral cells, and finally the merging of the tetrahedral cells into polyhedrons. The growth rates of the surface cells and the cell volume are specified are assigned (1.15). This was chosen as a compromise to allow the cells to grow slowly, and to obtain a low cell count. The resulting mesh was checked for skewness and orthogonality prior to running the simulation, to avoid divergence.

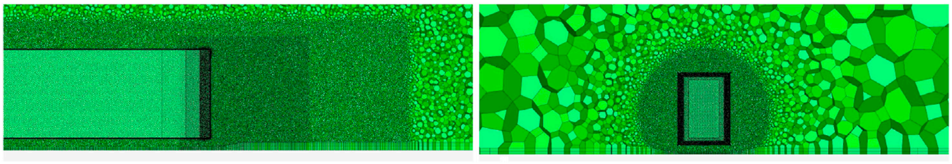

(a) (b)

Fig. 14. (Colour online) (a) Longitudinal cross-section of the polyhedral mesh used for PANS - ABS case in the near-wake region, and (b) lateral cross-section of the mesh in the vicinity of the GTS model.

Shown in Fig. 14(a) and (b) are the cross-sectional views of the polyhedral mesh in the longitudinal and lateral planes, respectively. The images show the concentration of the cells in the vicinity of the base of the GTS. Three cylindrical refinement zones of constant cell sizes encapsulate the GTS, and a growth rate is assigned for the cell volume in the outer regions. The cells expand in size from the refinement region to the boundaries of the domain. The final cell count was approximately 5.5 million elements, and the number of internal faces was in excess of 34 million, which increased the computational time significantly. For comparison, the hexahedral mesh with the highest cell count (fine mesh) of approximately 10.78 million elements had 32 million internal faces. Similar meshes have previously been constructed for the flow analysis of an Ahmed body using PANS equations (see Rao et al. (2018a)).

Appendix B. $k - \varepsilon$ turbulence model

Simulations using the RANS two equation $k - \varepsilon$ turbulence model were undertaken for the GTS model. AVL SMART Bounded scheme was used for the momentum equations while MINMOD Bounded scheme was used for the turbulence equations. The convergence criteria of the velocity, pressure and the turbulence quantities were set to 10^{-6}. Fig. 15(a) and 15(b) show the velocity contours in the vertical midplane at the rear of the GTS model for gap heights of $G/H = 0.14$ (the fine mesh was used), and $G/H = 1.1$, respectively. In both cases, symmetrical distribution of the vortices is observed at $0.14H$, and a slight asymmetry is observed when the GTS model is at a height of $1.1H$, with the larger vortex being located above the lateral midplane and the saddle point is at a height lower than the lateral midplane, similar to that observed in flow state II. In both cases, the line joining the centres of the vortices is nearly parallel to the vertical edge of the base, and does not predict a strong asymmetry as observed in the experimental studies and the unsteady numerical simulations.

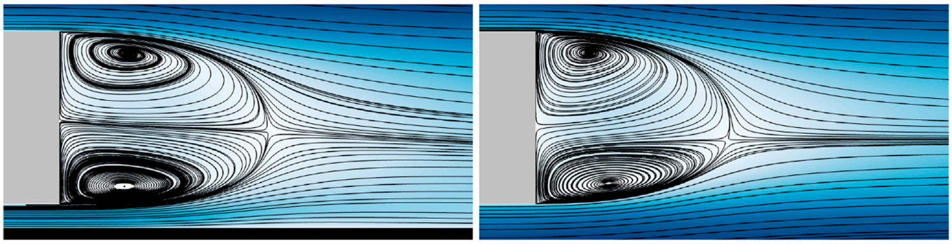
(a) (b)

Fig. 15. (Colour online) Visualisation of the contours of the normalised velocity overlaid with streamlines in the vertical midplane at the rear of the GTS at a gap height of (a) $G/H = 0.14$ and (b) $G/H = 1.1$ performed using the $k - \varepsilon$ turbulence model. Contour shading as per Fig. 4. Flow is from left to right in these images.

Appendix C

C.1 Computation of the dynamic parameter (f_k)

The f_k parameter is dynamically computed at every time-step in the PANS simulations (Basara et al. (2011); Krajnović et al. (2012b); Girimaji and Abdol-Hamid (2005)). The input f_k is derived from the numerical formulation is given by:

$$\text{input}\, f_k = \frac{1}{\sqrt{C_\mu}}\left(\frac{\Delta}{\Lambda}\right)^{2/3} \tag{1}$$

where, $C_\mu = 0.22$, $\Delta = k^{3/2}/\varepsilon$, and Λ is the geometric averaged grid spacing in the three directions. Here, k is the turbulent kinetic energy and ε is the dissipation rate of k.

The output f_k is computed by the ratio of the unresolved kinetic energy ($k_{unresolved}$) to the total kinetic energy ($k_{total} = k_{unresolved} + k_{resolved}$):

$$\text{output}\, f_k = k_{unresolved}/(k_{unresolved} + k_{resolved}) \tag{2}$$

The other dynamic parameter is the ratio of the unresolved-to-total dissipation, denoted by f_ε. Here, the equality $\varepsilon_u = \varepsilon_{total}$ is assumed, resulting $f_\varepsilon = 1$. For the derivation of the PANS equations, the reader is referred to Basara et al. (2011) and Jakirlic et al. (2017a).

In sections C.2 - C.14, the contours of the time-averaged velocity in the near wake is shown in subfigure (a), the contours of instantaneous input and output f_k are shown in subfigures (b) and (c), respectively, and the averaged output f_k is shown in subfigure (d). Figs. 16–26 show the contours of time-averaged flow and the f_k contours for the Ground Transportation System (GTS) at a gap height of $0.14H$, while the same contours are shown for the GTS at a gap height of $1.1H$ in Figs. 27 and 28.

For most bluff body flows investigated previously, the input f_k was usually a conservative estimate compared to the resulting output f_k. However, in the current study, the contours of the output f_k in the near wake are higher than that observed for the input f_k for the GTS at $G/H = 0.14$. At first, this may indicate a large amount of unresolved kinetic energy in the near wake, but on closer examination of the contours of the unresolved and the total kinetic energy in the wake (Figs. 29 and 30), the values of both the resolved and unresolved kinetic energy are low; thereby, values of output f_k are higher. The values of the unresolved kinetic energy in the region of the large triangular-shaped vortex are significantly lower as compared to other parts of the wake, while that around the smaller elliptical-shaped vortex are higher. This indicates that the triangular-shaped vortex is more stable (also see McArthur et al. (2016)), while higher energy content of the flow resides in regions around the elliptical-shaped vortex, saddle point and further downstream. It may be noted that PANS - ASB/ASR schemes result in flow state I topology, while PANS - CDS results in an anti-symmetric flow topology - flow state II. Also discernible in these figures is the decrease in the unresolved kinetic energy in the wake with an increase in the spatial resolution of the mesh.

At a gap height of $G/H = 1.1$, both the input and output f_k contours are lower, primarily on account of the unresolved kinetic energy being two orders of magnitude lower as compared to the total kinetic energy, thereby resulting in very low values of the output f_k. In such cases, there is insufficient turbulence modelling, and the numerical scheme plays a larger role (Krajnović et al. (2016b); Basara et al. (2018); Pereira et al. (2018b)). Furthermore, the values of the unresolved kinetic energy are much lower when PANS - CDS is used as compared to the PANS - ASB scheme. The PANS - CDS accurately predicts the flow asymmetry, with a flow state II topology, similar to that observed in the LES of Rao et al. (2018b). The contours of the kinetic energy are shown in Fig. 31 for both these cases.

C.2 $G/H = 0.14$ - Coarse mesh - ASB

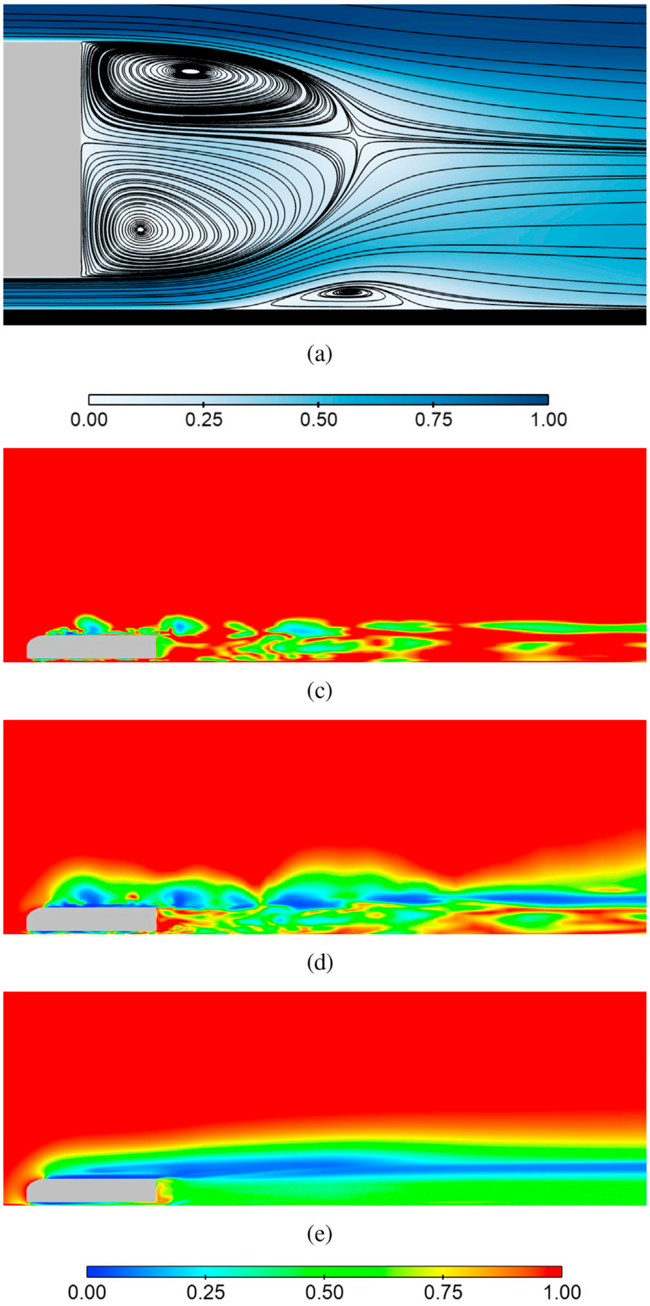

Fig. 16. (a) Visualisation of the contours of the normalised time-averaged velocity overlaid with streamlines. Contours of (b) input f_k, (c) output f_k, (d) averaged output f_k. Flow is from left to right in these images.

C.3 $G/H = 0.14$ - Coarse mesh - ASR

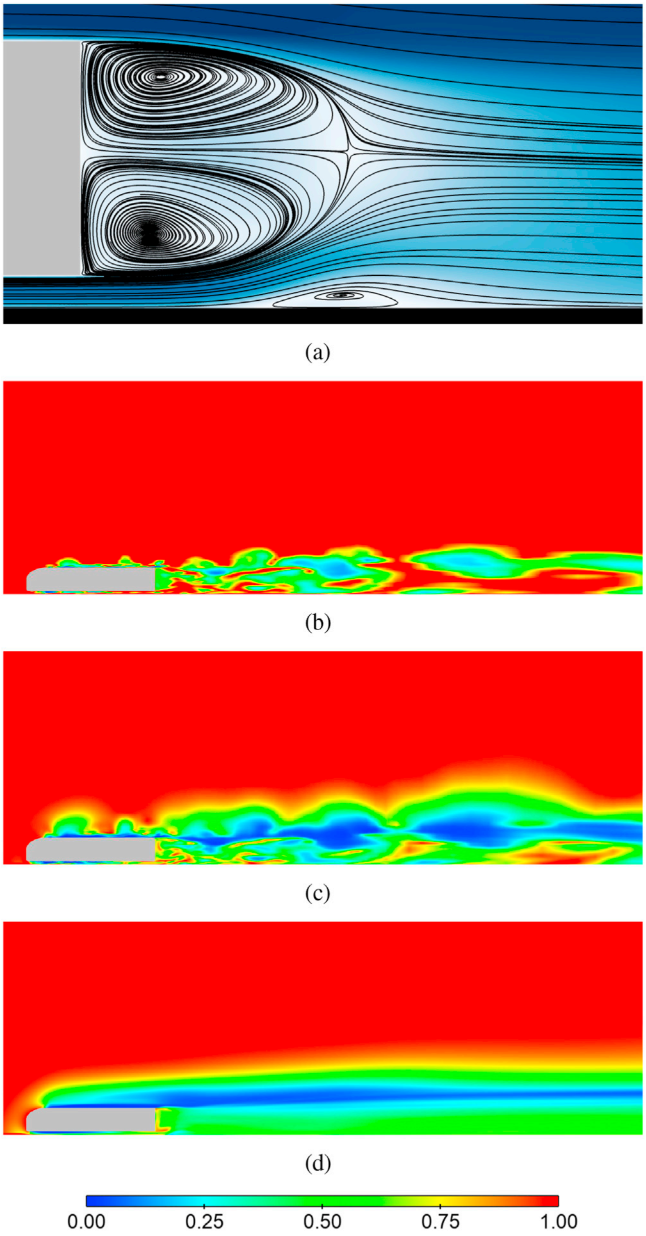
(a)

(b)

(c)

(d)

Fig. 17. (a) Visualisation of the contours of the normalised time-averaged velocity overlaid with streamlines. Contours of (b) input f_k, (c) output f_k, (d) averaged output f_k. Flow is from left to right in these images.

C.4 $G/H = 0.14$ - Coarse mesh - CDS

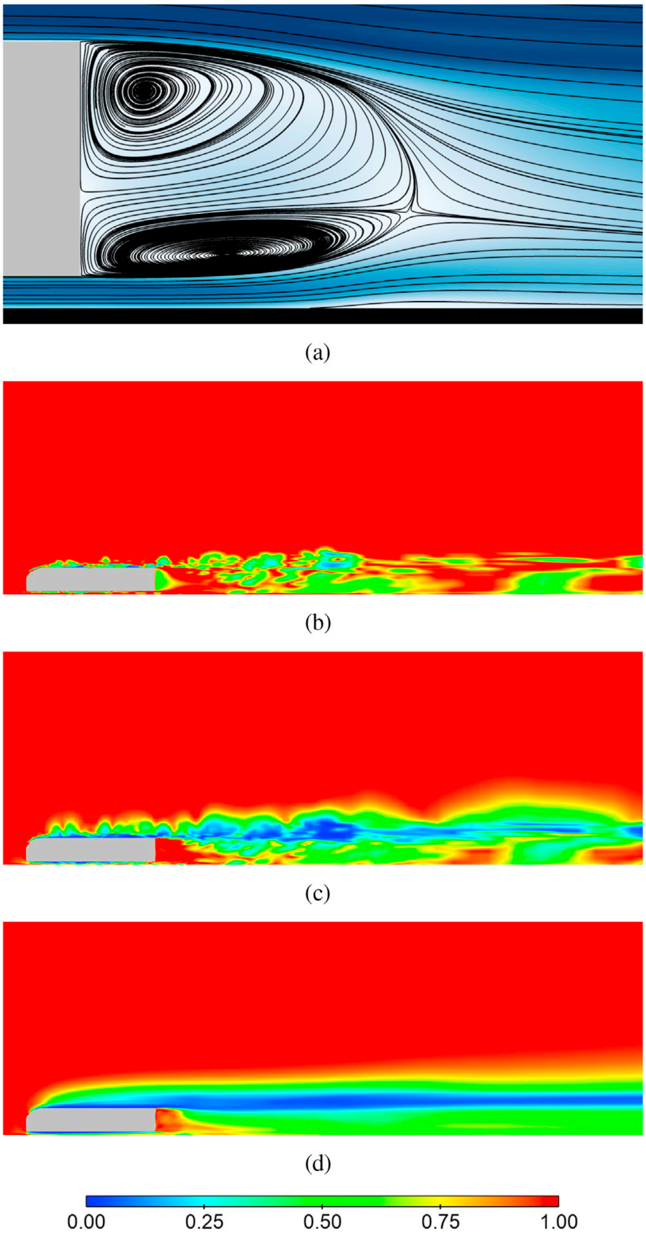

(a)

(b)

(c)

(d)

Fig. 18. (a) Visualisation of the contours of the normalised time-averaged velocity overlaid with streamlines. Contours of (b) input f_k, (c) output f_k, (d) averaged output f_k. Flow is from left to right in these images.

C.5 $G/H = 0.14$ - Medium mesh - ASB

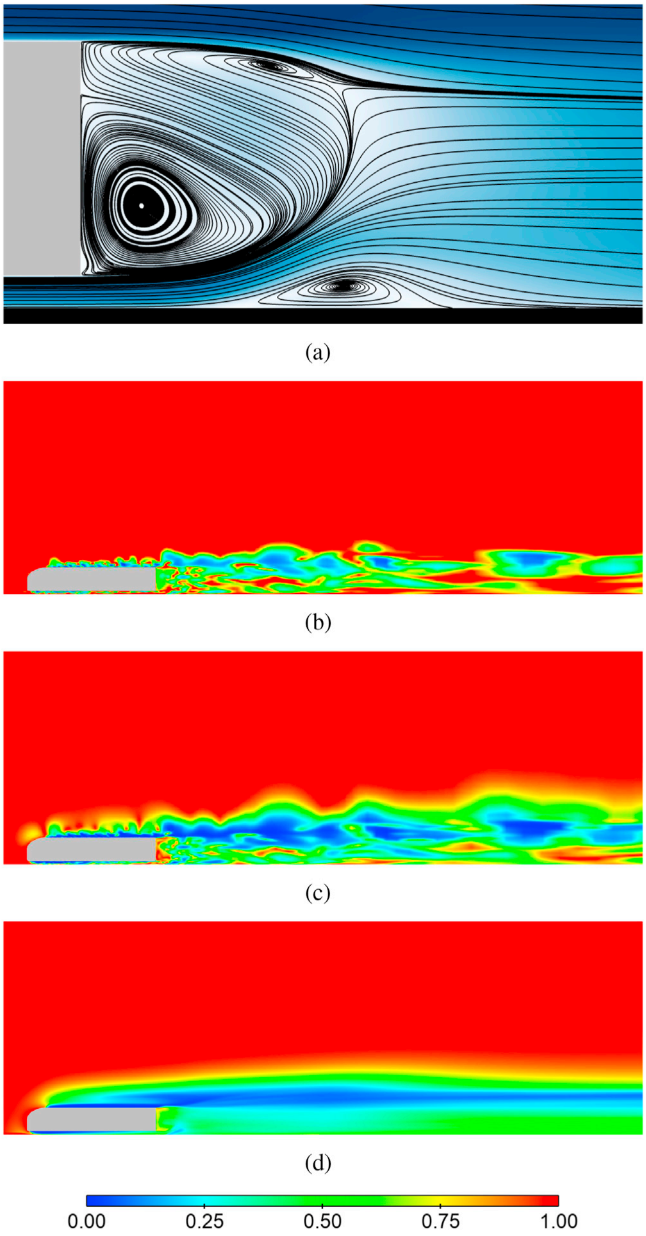

Fig. 19. (a) Visualisation of the contours of the normalised time-averaged velocity overlaid with streamlines. Contours of (b) input f_k, (c) output f_k, (d) averaged output f_k. Flow is from left to right in these images.

C.6 $G/H = 0.14$ - Medium mesh - ASR

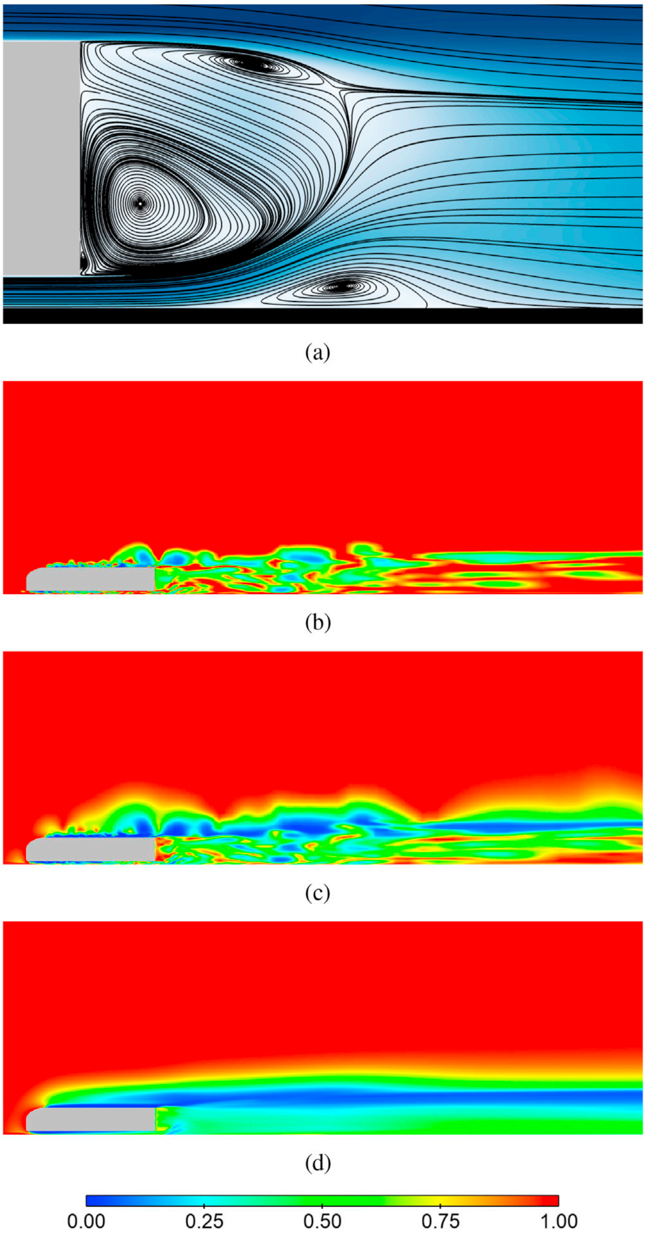

Fig. 20. (a) Visualisation of the contours of the normalised time-averaged velocity overlaid with streamlines. Contours of (b) input f_k, (c) output f_k, (d) averaged output f_k. Flow is from left to right in these images.

C.7 $G/H = 0.14$ - Medium mesh - CDS

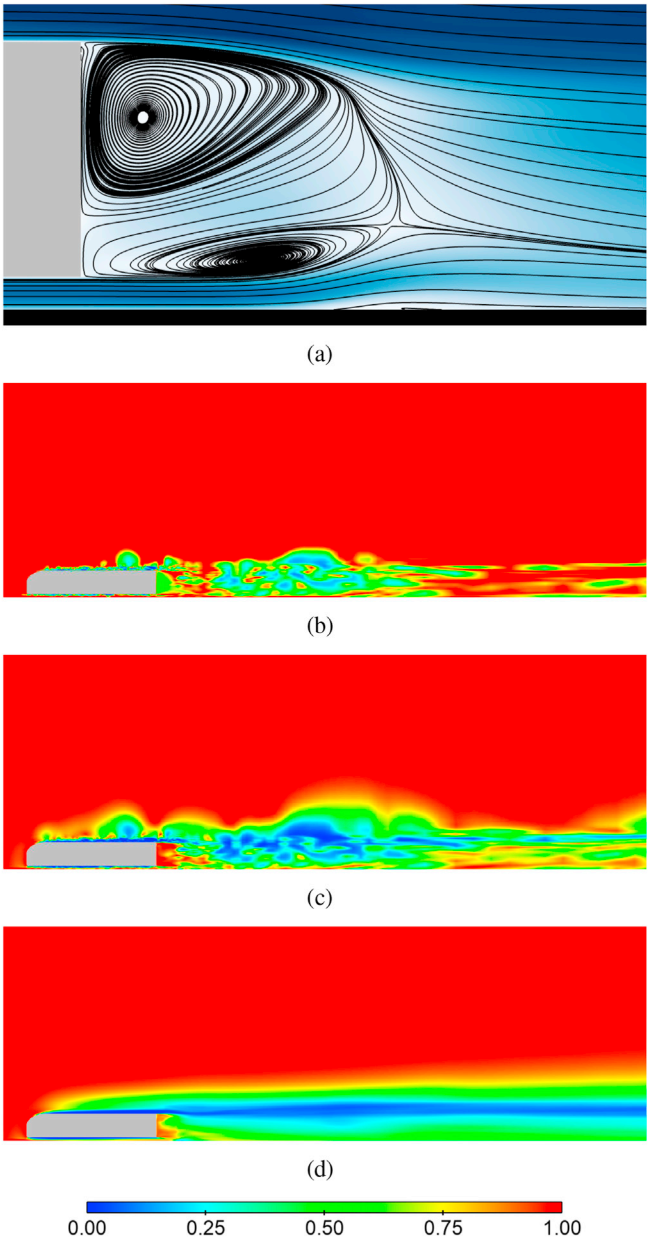

Fig. 21. (a) Visualisation of the contours of the normalised time-averaged velocity overlaid with streamlines. Contours of (b) input f_k, (c) output f_k, (d) averaged output f_k. Flow is from left to right in these images.

C.8 $G/H = 0.14$ - Fine mesh - ASB

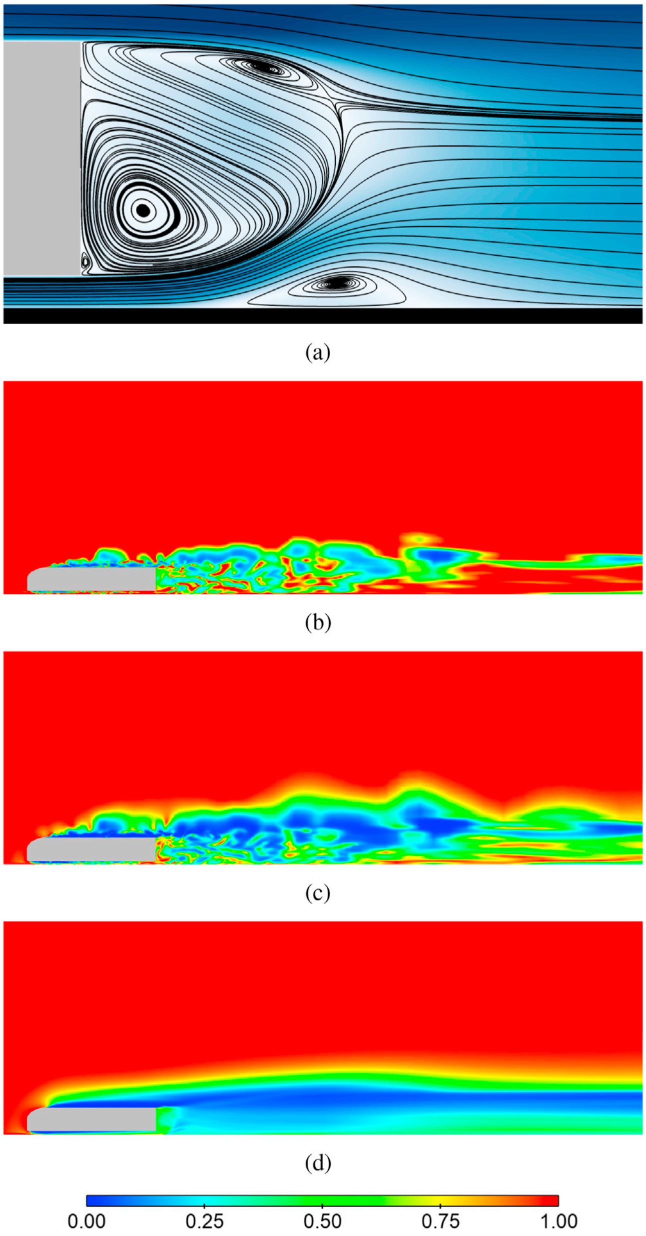

Fig. 22. (a) Visualisation of the contours of the normalised time-averaged velocity overlaid with streamlines. Contours of (b) input f_k, (c) output f_k, (d) averaged output f_k. Flow is from left to right in these images.

C.9 $G/H = 0.14$ - Fine mesh - CDS

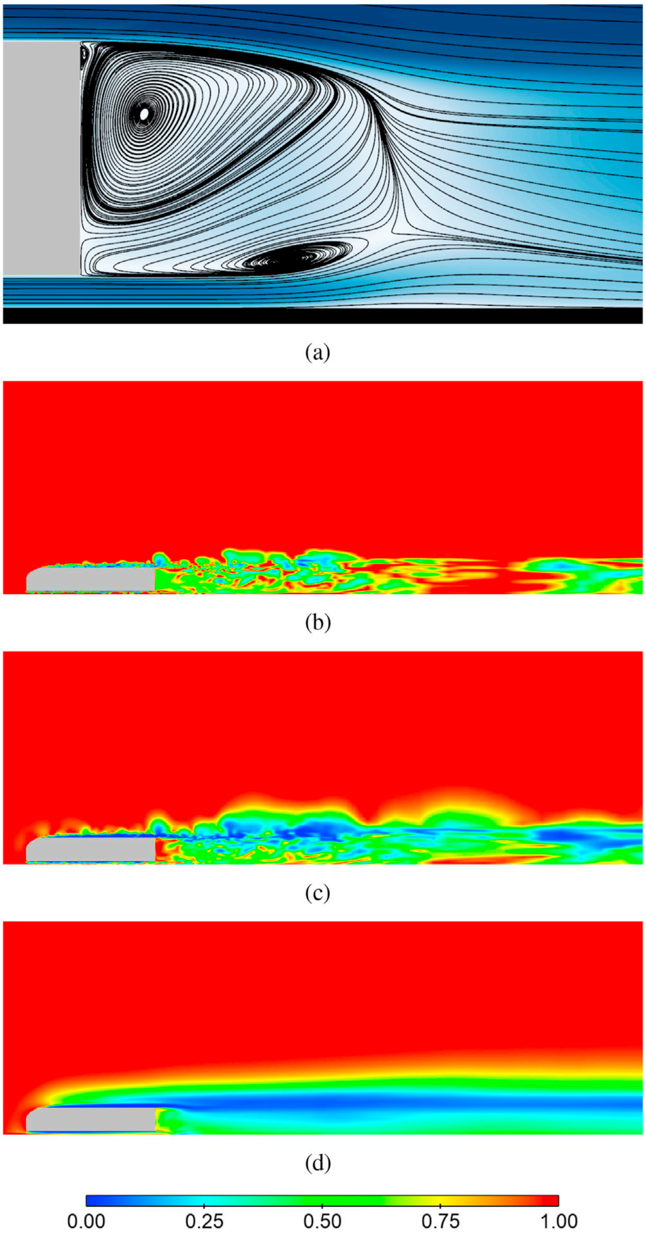
(a)

(b)

(c)

(d)

Fig. 23. (a) Visualisation of the contours of the normalised time-averaged velocity overlaid with streamlines. Contours of (b) input f_k, (c) output f_k, (d) averaged output f_k. Flow is from left to right in these images.

C.10 $G/H = 0.14$ - Fine mesh - ASB → CDS

The flow topology changed from state I to flow state II after the numerical scheme was changed from ASB to CDS. The saved solution from PANS - ASB was restarted with the CDS scheme, and the averaging of the flow quantities commenced after a time equivalent to 1.5 flow passes through the domain had elapsed. The contours of the mean flow and the dynamic parameter were then averaged for a time equivalent to 7.5 through-flows and are presented here.

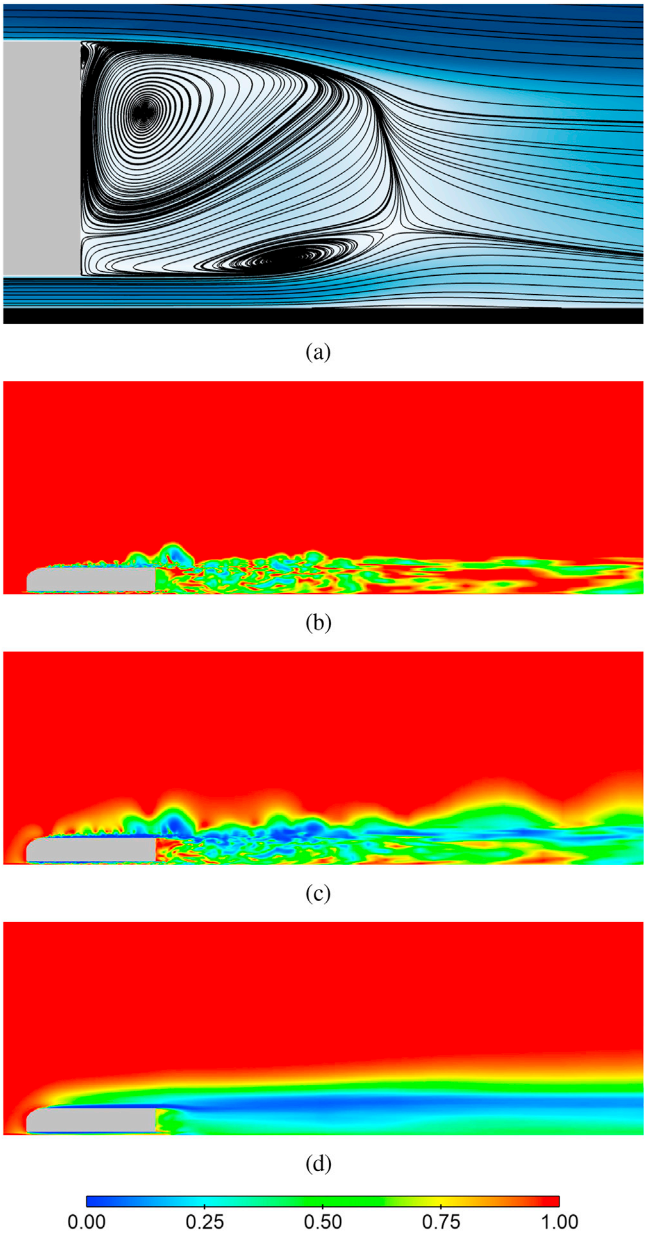

Fig. 24. (a) Visualisation of the contours of the normalised time-averaged velocity overlaid with streamlines. Contours of (b) input f_k, (c) output f_k, (d) averaged output f_k. Flow is from left to right in these images.

C.11 $G/H = 0.14$ - Fine mesh - CDS → ASB

The flow topology changed from state II to flow state I after the numerical scheme was changed from CDS to ASB. The saved solution from PANS - CDS was restarted with the ASB scheme, and the averaging of the flow quantities commenced after 8 flow passes through the domain. The contours of the mean flow and the dynamic parameter were then averaged for a time equivalent to 4 through-flows and are presented here.

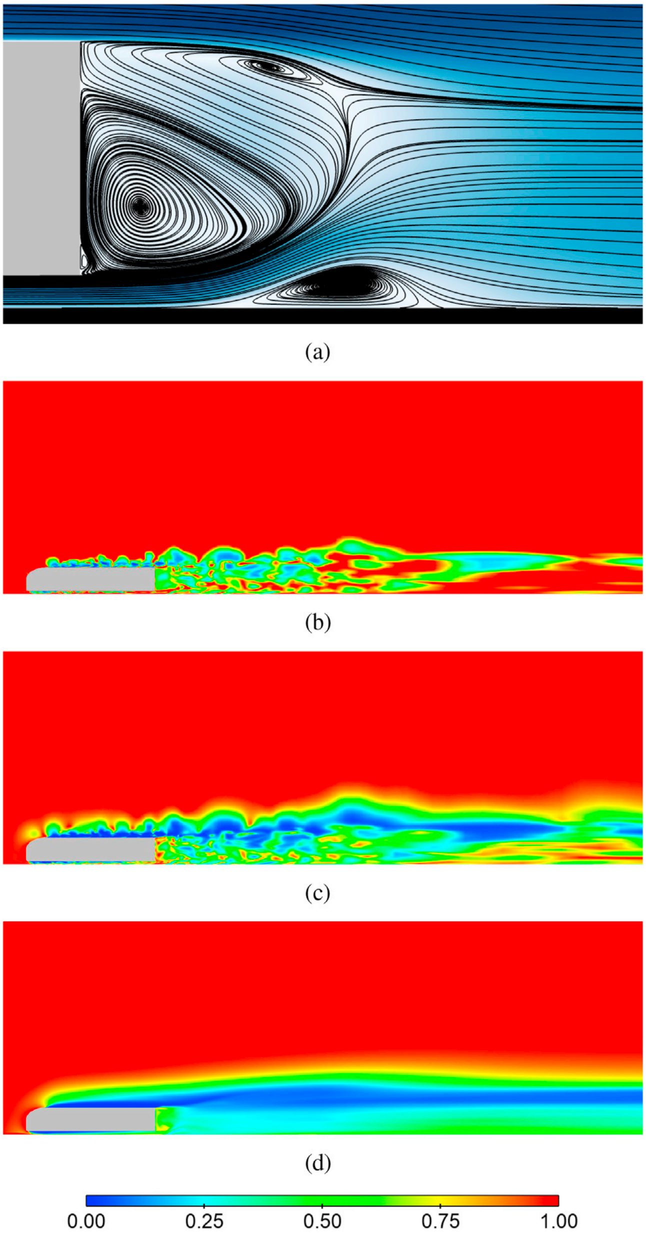
(a)

(b)

(c)

(d)

Fig. 25. (a) Visualisation of the contours of the normalised time-averaged velocity overlaid with streamlines. Contours of (b) input f_k, (c) output f_k, (d) averaged output f_k. Flow is from left to right in these images.

C.12 $G/H = 0.14$ - Polyhedral mesh - ASB

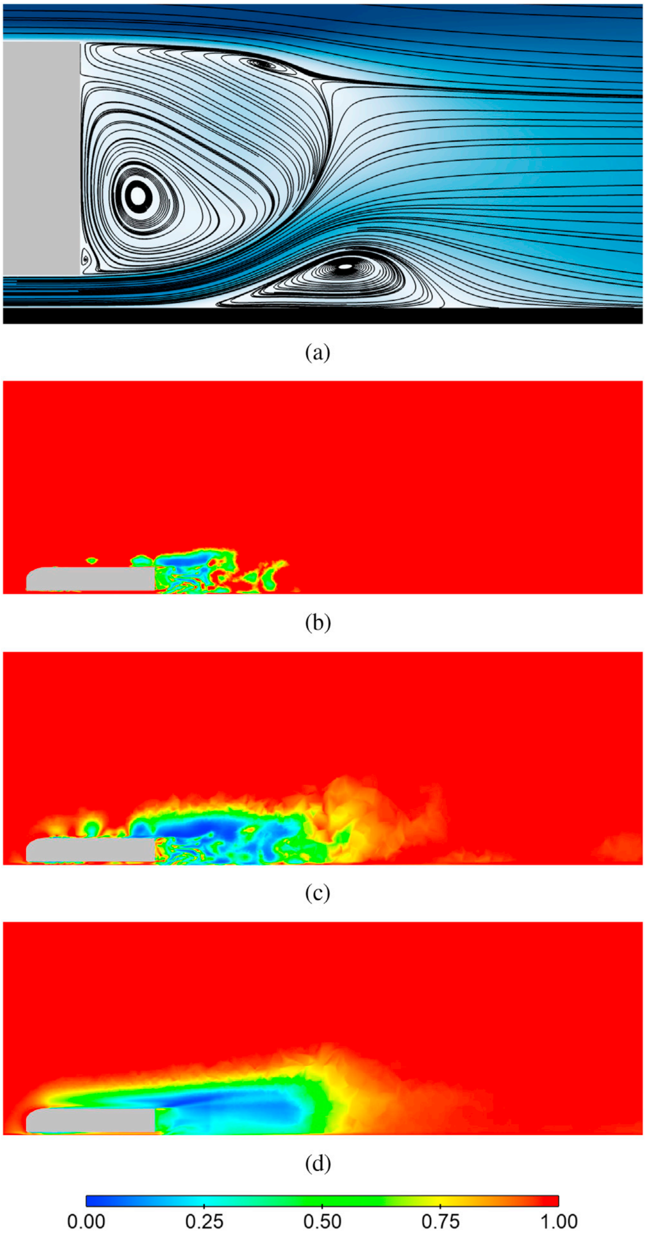
(a)

(b)

(c)

(d)

Fig. 26. (a) Visualisation of the contours of the normalised time-averaged velocity overlaid with streamlines. Contours of (b) input f_k, (c) output f_k, (d) averaged output f_k. Flow is from left to right in these images.

C.13 $G/H = 1.1$ - ASB

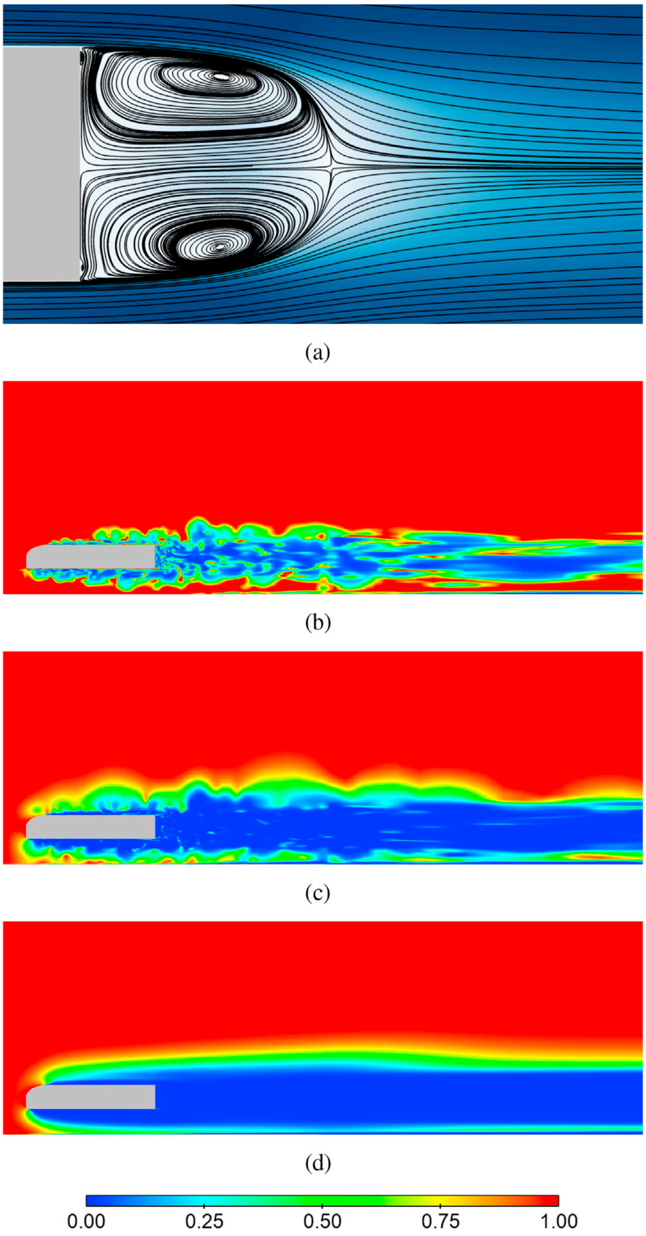
(a)

(b)

(c)

(d)

Fig. 27. (a) Visualisation of the contours of the normalised time-averaged velocity overlaid with streamlines. Contours of (b) input f_k, (c) output f_k, (d) averaged output f_k. Flow is from left to right in these images.

C.14 $G/H = 1.1$ - CDS

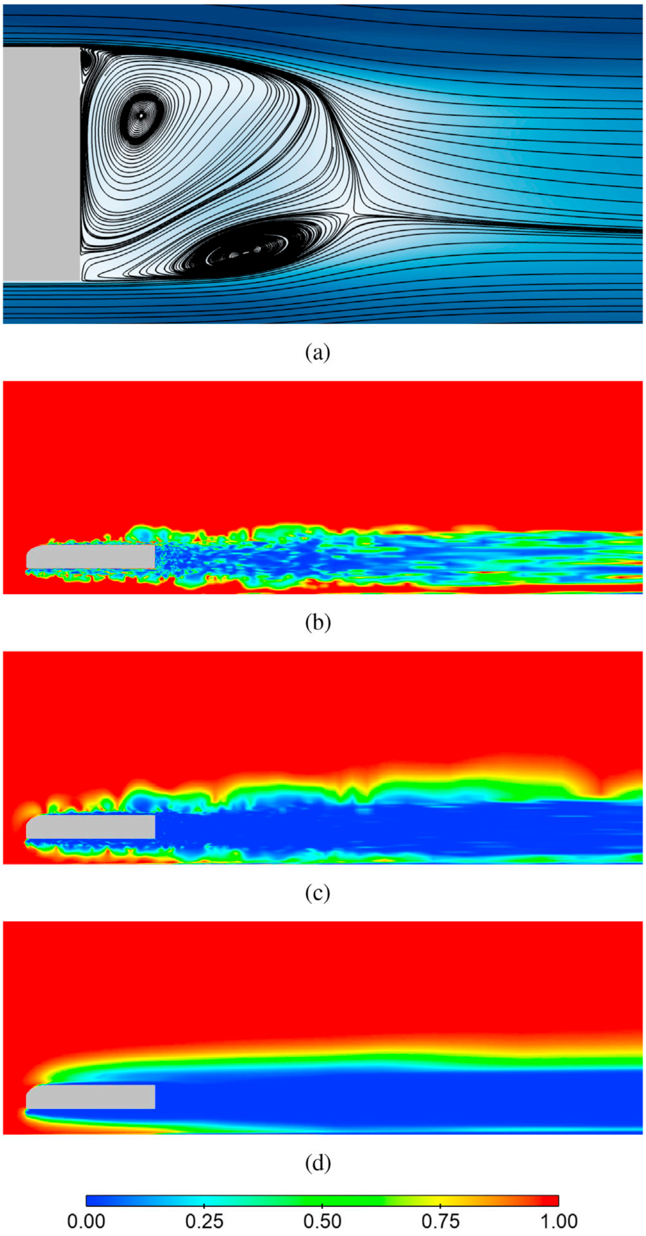
(a)

(b)

(c)

(d)

Fig. 28. (a) Visualisation of the contours of the normalised time-averaged velocity overlaid with streamlines. Contours of (b) input f_k, (c) output f_k, (d) averaged output f_k. Flow is from left to right in these images.

C.15 Contours of $k_{unresolved}$ and k_{total}

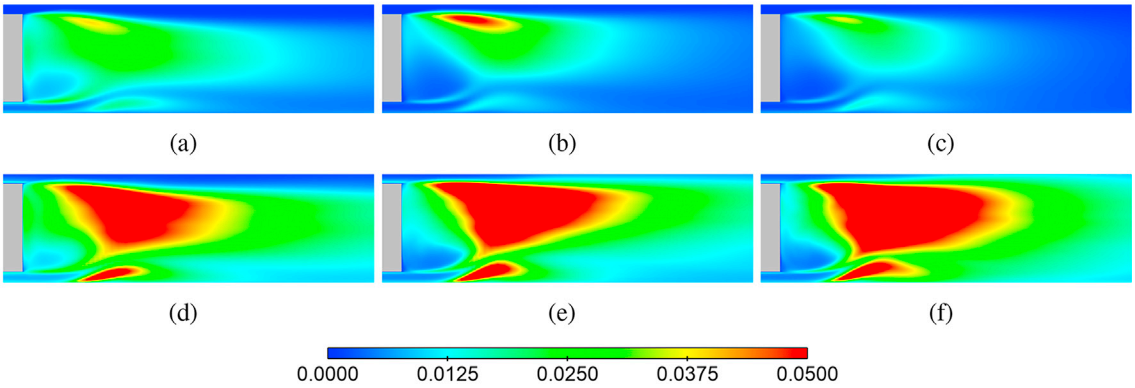
(a)

(b)

(c)

(d)

(e)

(f)

Fig. 29. Contours of the unresolved kinetic energy (a)–(c), and total kinetic energy (d)–(f) in the near wake of the GTS for PANS - ASB for the GTS model at $G/H = 0.14$. Left column - coarse mesh, middle column - medium mesh and right column - fine mesh. Flow is from left to right in these images.

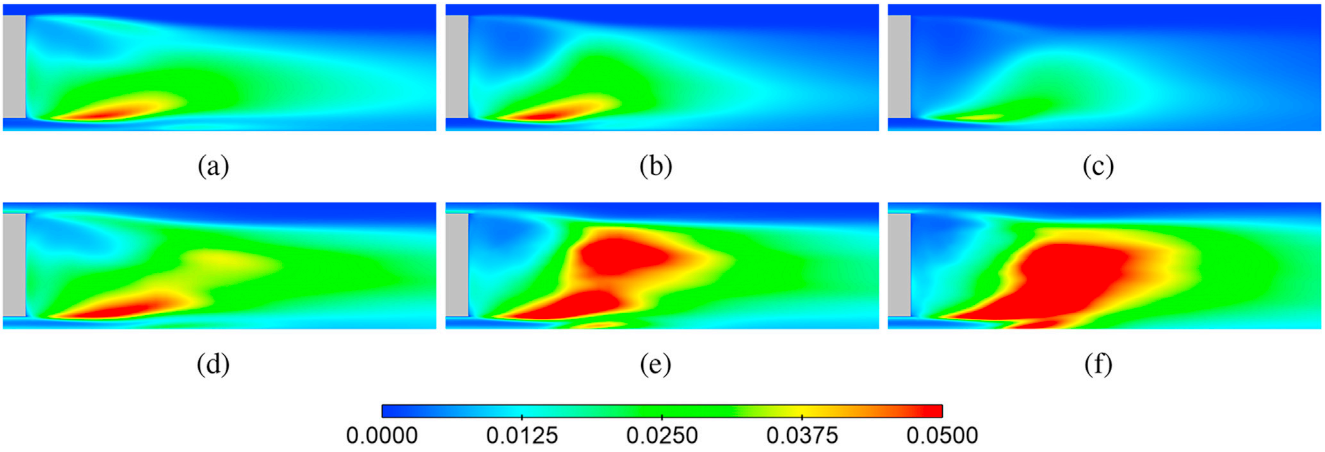

Fig. 30. Contours of the unresolved kinetic energy (a)–(c), and total kinetic energy (d)–(f) in the near wake of the GTS for PANS - CDS for the GTS model at $G/H = 0.14$. Left column - coarse mesh, middle column - medium mesh and right column - fine mesh. Flow is from left to right in these images.

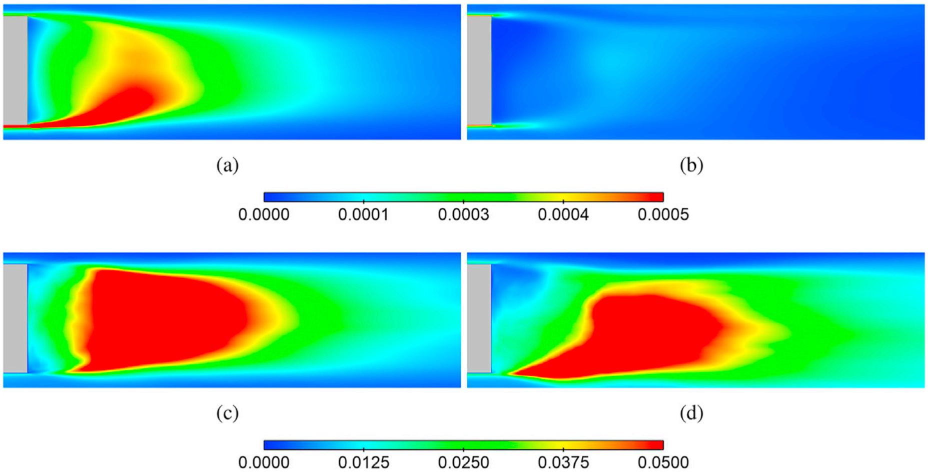

Fig. 31. Contours of the unresolved kinetic energy (a)–(b), and total kinetic energy (c)–(d) in the near wake of the GTS at $G/H = 1.1$. Left column - PANS - ASB and right column PANS - CDS. Flow is from left to right in these images.

References

Adedoyin, A.A., Walters, D.K., Bhushan, S., 2015. Investigation of turbulence model and numerical scheme combinations for practical finite-volume large eddy simulations. Eng. Appl. Comput. Fluid Mech. 9, 324–342. https://doi.org/10.1080/19942060.2015.1028151.

Ahmed, S.R., Ramm, G., Faltin, G., 1984. Some salient features of the time-averaged ground vehicle wake. In: SAE Technical Paper, 840300. SAE International.

Aljure, D.E., Calafell, J., Baez, A., Oliva, A., 2018. Flow over a realistic car model: wall modeled large eddy simulations assessment and unsteady effects. J. Wind Eng. Ind. Aerod. 174, 225–240.

Ashton, N., West, A., Lardeau, S., Revell, A., 2016. Assessment of RANS and DES methods for realistic automotive models. Comput. Fluids 128, 1–15.

Aubin, J., Fletcher, D.F., Xuereb, C., 2004. Modeling turbulent flow in stirred tanks with CFD: the influence of the modeling approach, turbulence model and numerical scheme. Exp. Therm. Fluid Sci. 28, 431–445, 5th international conference on Gas-Liquid and Gas-Liquid-Solid Reactor Engineering.

AVL, 2014. FIRE™ M User Manual. AVL GmbH, Graz, Austria.

Barros, D., Borée, J., Cadot, O., Spohn, A., Noack, B.R., 2017a. Forcing symmetry exchanges and flow reversals in turbulent wakes. J. Fluid Mech. 829.

Barros, D., Borée, J., Noack, B.R., Spohn, A., Ruiz, T., 2017b. Effects of Unsteady Coanda Blowing on the Wake and Drag of a Simplified Blunt Vehicle. Springer International Publishing, Cham, pp. 365–373.

Basara, B., 2004. Employment of the second-moment turbulence closure on arbitrary unstructured grids. Int. J. Numer. Methods Fluid. 44.

Basara, B., 2015a. Fluid flow and conjugate heat transfer in a matrix of surface-mounted cubes: a PANS study. Int. J. Heat Fluid Flow 51, 166–174. Theme special issue celebrating the 75th birthdays of Brian Launder and Kemo Hanjalic.

Basara, B., 2015b. PANS method as a computational framework from an industrial perspective. In: Progress in Hybrid RANS-LES Modelling. Springer International Publishing, Cham, pp. 3–17.

Basara, B., Krajnović, S., Girimaji, S.S., Pavlovic, Z., 2011. Near-wall formulation of the partially averaged Navier–Stokes turbulence model. AIAA 49, 2627–2636.

Basara, B., Pavlovic, Z., Krajnović, S., 2018. Effects of convection schemes on Hybrid RANS-LES calculations. In: Progress in Hybrid RANS-LES Modelling. Springer International Publishing, pp. 145–155.

Baxevanou, C.A., Vlachos, N.S., 2004. A comparative study of numerical schemes and turbulence models for wind turbine aerodynamics modelling. Wind Eng. 28, 275–290. https://doi.org/10.1260/0309524041590134.

Bonnavion, G., Cadot, O., 2018. Unstable wake dynamics of rectangular flat-backed bluff bodies with inclination and ground proximity. J. Fluid Mech. 854, 196232.

Brackston, R.D., Garca de la Cruz, J.M., Wynn, A., Rigas, G., Morrison, J.F., 2016. Stochastic modelling and feedback control of bistability in a turbulent bluff body wake. J. Fluid Mech. 802, 726749.

Bruneau, C.H., Creusé, E., Depeyras, D., Gilliéron, P., Mortazavi, I., 2010. Coupling active and passive techniques to control the flow past the square back Ahmed body. Comput. Fluids 39, 1875–1892.

Cadot, O., Evrard, A., Pastur, L., 2015. Imperfect supercritical bifurcation in a three-dimensional turbulent wake. Phys. Rev. E 91, 063005.

Castelain, T., Michard, M., Szmigiel, M., Chacaton, D., Juvé, D., 2018. Identification of flow classes in the wake of a simplified truck model depending on the underbody velocity. J. Wind Eng. Ind. Aerod. 175, 352–363.

Croll, R.H., Gutierrez, W.T., Hassan, B., Suazo, J.E., Riggins, A.J., 1996. Experimental investigation of the ground transportation systems (GTS) project for heavy vehicle drag reduction. In: SAE Technical Paper. SAE International, pp. 237–259.

Dalla Longa, L., Evstafyeva, O., Morgans, A.S., 2017. Bi-modality in the wakes of simplified road vehicles: simulation and feedback control. In: 52nd 3AF International Conference on Applied Aerodynamics, Lyon, France, 27 29 March 2017, pp. 1–6.

Davidson, L., 7 Sep 2018. Fluid Mechanics, Turbulent Flow and Turbulence Modeling. http://www.tfd.chalmers.se/~lada/postscript_files/solids-and-fluids_turbulent-flow_turbulence-modelling.pdf.

El-Alti, M., Chernoray, V., Kjellgren, P., Hjelm, L., Davidson, L., 2016. Computations and Full-scale Tests of Active Flow Control Applied on a Volvo Truck-trailer. Springer International Publishing, Cham, pp. 253–267.

Engels, T., Kolomenskiy, D., Schneider, K., Farge, M., Lehmann, F.O., Sesterhenn, J., 2018. Helical vortices generated by flapping wings of bumblebees. Fluid Dynam. Res. 50, 011419.

Eulalie, Y., Gilotte, P., Mortazavi, I., 2017. Numerical study of flow control strategies for a simplified square back ground vehicle. Fluid Dynam. Res. 49, 035502.

Evrard, A., Cadot, O., Herbert, V., Ricot, D., Vigneron, R., Délery, J., 2016. Fluid force and symmetry breaking modes of a 3D bluff body with a base cavity. J. Fluid Struct. 61, 99–114.

Evstafyeva, O., Morgans, A.S., Dalla Longa, L., 2017. Simulation and feedback control of the Ahmed body flow exhibiting symmetry breaking behaviour. J. Fluid Mech. 817.

Gaskell, P.H., Lau, A.K.C., 1988. Curvature-compensated convective transport: srt, a new boundedness- preserving transport algorithm. Int. J. Numer. Methods Fluid. 8, 617–641.

Gentile, V., van Oudheusden, B.W., Schrijer, F.F.J., Scarano, F., 2017. The effect of angular misalignment on low-frequency axisymmetric wake instability. J. Fluid Mech. 813.

Ghias, R., Khondge, A., Sovani, S.D., 2008. Flow simulations around a generic ground transportation system: using immersed boundary method. In: Commercial Vehicle Engineering Congress & Exhibition. SAE International.

Girimaji, S., Abdol-Hamid, K., 2005. Partially-averaged Navier–Stokes Model for Turbulence: Implementation and Validation. American Institute of Aeronautics and Astronautics, Reno, Nevada, pp. 1–14.

Girimaji, S.S., 2006. Partially-Averaged Navier–Stokes model for turbulence: a Reynolds-Averaged Navier–Stokes to direct numerical simulation bridging method. J. Appl. Mech. Trans. ASME 73, 413–421.

Girimaji, S.S., Jeong, E., Srinivasan, R., 2005. Partially Averaged Navier–Stokes method for turbulence: fixed point analysis and comparison with unsteady partially averaged Navier–Stokes. J. Appl. Mech. 73, 422–429.

Girimaji, S.S., Suman, S., 2012. Partially averaged Navier–Stokes (PANS) method for turbulence simulations: theory and practice. In: Progress in Hybrid RANS-LES Modelling. Springer, Berlin, Heidelberg, pp. 29–43.

Grandemange, M., Cadot, O., Courbois, A., Herbert, V., Ricot, D., Ruiz, T., Vigneron, R., 2015. A study of wake effects on the drag of Ahmed's squareback model at the industrial scale. J. Wind Eng. Ind. Aerod. 145, 282–291.

Grandemange, M., Cadot, O., Gohlke, M., 2012. Reflectional symmetry breaking of the separated flow over three-dimensional bluff bodies. Phys. Rev. E 86, 035302.

Grandemange, M., Gohlke, M., Cadot, O., 2013a. Bi-stability in the turbulent wake past parallelepiped bodies with various aspect ratios and wall effects. Phys. Fluids 25, 095103.

Grandemange, M., Gohlke, M., Cadot, O., 2013b. Turbulent wake past a three-dimensional blunt body. Part 1. Global modes and bi-stability. J. Fluid Mech. 722, 5184.

Grandemange, M., Gohlke, M., Cadot, O., 2014. Turbulent wake past a three-dimensional blunt body. Part 2. Experimental sensitivity analysis. J. Fluid Mech. 752, 439–461.

Guilmineau, E., Deng, G.B., Leroyer, A., Queutey, P., Visonneau, M., Wackers, J., 2017. Assessment of hybrid RANS-LES formulations for flow simulation around the Ahmed body. Comput. Fluids. https://doi.org/10.1016/j.compfluid.2017.01.005. issn = 0045-7930.

Gunes, D., 2010. On the similarity of wind tunnel experiments and numerical simulation of heavy-duty trailer flow. Prog. Comput. Fluid Dynam. Int. J. 10, 168–176.

Haff, J., Jönsson, M., Loose, S., Wagner, C., 2017. Reliability of engineering methods in heavy-vehicle aerodynamics. In: SAE International Journal of Engines. SAE International, pp. 1–14.

Hanjalić, K., Popovac, M., Hadžiabdić, M., 2004. A robust near-wall elliptic-relaxation eddy-viscosity turbulence model for CFD. Int. J. Heat Fluid Flow 25, 1047–1051. Cited By 249.

Harten, A., 1983. High resolution schemes for hyperbolic conservation laws. J. Comput. Phys. 49, 357–393.

Herry, B.B., Keirsbulck, L., Labraga, L., Paquet, J.B., 2011. Flow bistability downstream of three-dimensional double backward facing steps at zero-degree sideslip. J. Fluid Eng. 133, 054501–054501–4.

Howell, J., Le Good, G., 2008. The effect of backlight aspect ratio on vortex and base drag for a simple car-like shape. In: SAE World Congress & Exhibition. SAE International, pp. 1–7.

Hunt, J.C.R., Hussain, F., 1991. A note on velocity, vorticity and helicity of inviscid fluid elements. J. Fluid Mech. 229, 569587.

Jakirlic, S., Kutej, L., Basara, B., Tropea, C., 2014. Computational study of the aerodynamics of a realistic car model by means of RANS and hybrid RANS/LES approaches. SAE Int. J. Passeng. Car Mech. Syst. 7, 559–574.

Jakirlic, S., Kutej, L., Hanssmann, D., Basara, B., Schütz, T., Tropea, C., 2016. Rear-end shape influence on the aerodynamic properties of a realistic car model: a RANS and Hybrid LES/RANS study. In: New Results in Numerical and Experimental Fluid Mechanics X: Contributions to the 19th STAB/DGLR Symposium Munich, Germany, 2014. Springer International Publishing, pp. 397–407.

Jakirlic, S., Kutej, L., Unterlechner, P., Tropea, C., 2017a. Critical assessment of some popular scale-resolving turbulence models for vehicle aerodynamics. SAE Int. J. Passeng. Car Mech. Syst. 10, 235–250.

Jakirlic, S., Kutej, L., Unterlechner, P., Tropea, C., 2017b. Critical assessment of some popular scale-resolving turbulence models for vehicle aerodynamics. SAE Int. J. Passeng. Cars - Mech. Syst. 10, 235–250.

Jakirlic, S., Maduta, R., 2015. Extending the bounds of 'steady' RANS closures: toward an instability-sensitive Reynolds stress model. Int. J. Heat Fluid Flow 51, 175–194. Theme special issue celebrating the 75th birthdays of Brian Launder and Kemo Hanjalic.

Jeong, J., Hussain, F., 1995. On the identification of a vortex. J. Fluid Mech. 285, 6994.

Kaiser, E., Noack, B.R., Cordier, L., Spohn, A., Segond, M., Abel, M., Daviller, G., Östh, J., Krajnović, S., Niven, R.K., 2014. Cluster-based reduced-order modelling of a mixing layer. J. Fluid Mech. 754, 365414.

Krajnović, S., Davidson, L., 2003. Numerical study of the flow around a bus-shaped body. J. Fluid Eng. 125, 500–509.

Krajnović, S., Lárusson, R., 2012. Large eddy simulations of the flow around pyramids. In: CFD Society of Canada Conference, pp. 1–8.

Krajnović, S., Lárusson, R., Basara, B., 2012a. Superiority of PANS compared to LES in predicting a rudimentary landing gear flow with affordable meshes. Int. J. Heat Fluid Flow 37, 109–122.

Krajnović, S., Minelli, G., Basara, B., 2016. Partially-Averaged Navier–Stokes simulations of two bluff body flows. Appl. Math. Comput. 272 (3), 692–706.

Krajnović, S., Ringqvist, P., Basara, B., 2012b. Comparison of PANS and LES simulations of the flow around a cuboid influenced by crosswind. In: Progress in Hybrid RANS-LES Modelling. Springer, Berlin, Heidelberg, pp. 205–217.

Lahaye, A., Leroy, A., Kourta, A., 2014. Aerodynamic characterisation of a square back bluff body flow. Int. J. Aerod. 4, 43–60.

Lakshmipathy, S., 2004. PANS Method of Turbulence: Simulation of High and Low Reynolds Number Flows Past a Circular Cylinder. Master's thesis. Texas A&M University.

Lakshmipathy, S., Reyes, D., Girimaji, S.S., 2011. Partially averaged Navier–Stokes method: modeling and simulation of low Reynolds number effects in flow past a circular cylinder. In: 6th Fluid Dynamics and Co-located Conferences. American Institute of Aeronautics and Astronautics, pp. 1–20. 0.

Levy, Y., Degani, D., Seginer, A., 1990. Graphical visualization of vortical flows by means of helicity. AIAA J. 28, 1347–1352.

Li, R., 2017. Aerodynamic Drag Reduction of a Square-back Car Model Using Linear Genetic Programming and Physic-based Control. Theses. ISAE-ENSMA Ecole Nationale Supérieure de Mécanique et d'Aérotechique - Poitiers.

Li, R., Barros, D., Borée, J., Cadot, O., Noack, B.R., Cordier, L., 2016. Feedback control of bimodal wake dynamics. Exp. Fluid 57, 158.

Li, R., Noack, B.R., Cordier, L., Borée, J., Harambat, F., 2017. Drag reduction of a car model by linear genetic programming control. Exp. Fluid 58, 103.

Lien, F.S., Leschziner, M.A., 1994. Upstream monotonic interpolation for scalar transport with application to complex turbulent flows. Int. J. Numer. Methods Fluid. 19, 527–548.

Lin, C.H., Lin, C.A., 1997. Simple high-order bounded convection scheme to model discontinuities. AIAA J. 35, 563–565.

Lo, K.H., Kontis, K., 2017. Flow around an articulated lorry model. Exp. Therm. Fluid Sci. 82, 58–74.

Lucas, J.M., Cadot, O., Herbert, V., Parpais, S., Délery, J., 2017. A numerical investigation of the asymmetric wake mode of a squareback Ahmed body effect of a base cavity. J. Fluid Mech. 831, 675697.

Ma, J.M., Peng, S.H., Davidson, L., Wang, F.J., 2011. A low Reynolds number variant of partially-averaged Navier–Stokes model for turbulence. Int. J. Heat Fluid Flow 32, 652–669.

Maleki, S., Burton, D., Thompson, M.C., 2017. Assessment of various turbulence models (ELES, SAS, URANS and RANS) for predicting the aerodynamics of freight train container wagons. J. Wind Eng. Ind. Aerod. 170, 68–80.

Mathey, F., Cokljat, D., Bertoglio, J.P., Sergent, E., 2006. Specification of LES inlet boundary condition using vortex method. Prog. Comput. Fluid Dynam. Int. J. 6, 58–67.

McArthur, D., Burton, D., Thompson, M.C., Sheridan, J., 2016. On the near wake of a simplified heavy vehicle. J. Fluid Struct. 66, 293–314.

McArthur, D., Burton, D., Thompson, M.C., Sheridan, J., 2018. An experimental characterisation of the wake of a detailed heavy vehicle in cross-wind. J. Wind Eng. Ind. Aerod. 175, 364–375.

Menter, F.R., Egorov, Y., 2010. The scale-adaptive simulation method for unsteady turbulent flow predictions. part 1: theory and model description. Flow, Turbul. Combust. 85, 113–138.

Minelli, G., Hartono, E.A., Chernoray, V., Hjelm, L., Basara, B., Krajnović, S., 2017. Validation of PANS and active flow control for a generic truck cabin. J. Wind Eng. Ind. Aerod. 171, 148–160.

Minelli, G., Krajnović, S., Basara, B., Noack, B.R., 2016. Numerical investigation of active flow control around a generic truck A-pillar. Flow, Turbul. Combust. 97, 1235–1254.

Minguez, M., Pasquetti, R., Serre, E., 2008. High-order large-eddy simulation of flow over the "Ahmed body" car model. Phys. Fluids 20, 095101.

Mirzaei, M., Krajnović, S., Basara, B., 2015. Partially-averaged Navier–Stokes simulations of flows around two different Ahmed bodies. Comput. Fluids 117, 273–286.

Moffatt, H.K., 1969. The degree of knottedness of tangled vortex lines. J. Fluid Mech. 35, 117129.

Moffatt, H.K., Tsinober, A., 1992. Helicity in laminar and turbulent flow. Annu. Rev. Fluid Mech. 24, 281–312.

Nakayama, A., Vengadesan, S.N., 2002. On the influence of numerical schemes and subgrid-stress models on large eddy simulation of turbulent flow past a square cylinder. Int. J. Numer. Methods Fluid. 38, 227–253. https://onlinelibrary.wiley.com/doi/pdf/10.1002/fld.214.

Ortega, J.M., Dunn, T., McCallen, R., Salari, K., 2004. Computational simulation of a heavy vehicle trailer wake. In: The Aerodynamics of Heavy Vehicles: Trucks, Buses, and Trains. Springer, pp. 219–233.

Östh, J., Krajnović, S., 2016. A LES study of a simplified tractor-trailer model. In: The Aerodynamics of Heavy Vehicles III. Springer, pp. 327–342.

Östh, J., Krajnović, S., Basara, B., 2010. LES study of breakdown control of A-pillar vortex. Int. J. Flow Contr. 2, 237–258.

Östh, J., Noack, B.R., Krajnović, S., Barros, D., Borée, J., 2014. On the need for a nonlinear subscale turbulence term in POD models as exemplified for a high-Reynolds-number flow over an Ahmed body. J. Fluid Mech. 747, 518544.

Park, N., Yoo, J.Y., Choi, H., 2004. Discretization errors in large eddy simulation: on the suitability of centered and upwind-biased compact difference schemes. J. Comput. Phys. 198, 580–616.

Pavia, G., Passmore, M., 2018. Characterisation of wake bi-stability for a square-back geometry with rotating wheels. In: Progress in Vehicle Aerodynamics and Thermal Management. Springer International Publishing, Cham, pp. 93–109.

Pavia, G., Passmore, M., Sardu, C., 2017. Evolution of the bi-stable wake of a square-back automotive shape. Exp. Fluid 59, 20.

Pereira, F.S., Eça, L., Vaz, G., Girimaji, S.S., 2018a. Challenges in Scale-Resolving Simulations of turbulent wake flows with coherent structures. J. Comput. Phys. 363, 98–115.

Pereira, F.S., Vaz, G., Eça, L., 2015. On the numerical requirements of RANS and hybrid turbulence models. In: VI International Conference on Computational Methods in Marine Engineering, pp. 1–17.

Pereira, F.S., Vaz, G., Eça, L., Girimaji, S.S., 2018b. Simulation of the flow around a circular cylinder at Re=3900 with Partially-Averaged Navier–Stokes equations. Int. J. Heat Fluid Flow 69, 234–246.

Perry, A.K., Pavia, G., Passmore, M., 2016. Influence of short rear end tapers on the wake of a simplified square-back vehicle: wake topology and rear drag. Exp. Fluid 57, 169.

Piomelli, U., Chasnov, J.R., 1996. Large-eddy Simulations: Theory and Applications. Springer Netherlands, Dordrecht, pp. 269–336.

Podvin, B., Sergent, A., 2015. A large-scale investigation of wind reversal in a square Rayleigh-Bénard cell. J. Fluid Mech. 766, 172–201.

Podvin, B., Sergent, A., 2017. Precursor for wind reversal in a square Rayleigh-Bénard cell. Phys. Rev. E 95, 013112.

Pržulj, V., 2016. An improved discretisation method for bounded convective schemes on unstructured co-located grid. In: ECCOS Congress 2016, VII European Congress on Computational Methods in Applied Sciences and Engineering, Crete Island, Greece, pp. 1–17.

Pržulj, V., Basara, B., 2001. Bounded convection schemes for unstructured grids. In: 15th AIAA Computational Fluid Dynamics Conference, Fluid Dynamics and Co-located Conferences. American Institute of Aeronautics and Astronautics, pp. 1–12.

Rao, A., Minelli, G., Basara, B., Krajnović, S., 2018a. On the two flow states in the wake of a hatchback Ahmed body. J. Wind Eng. Ind. Aerod. 173, 262–278.

Rao, A.N., Zhang, J., Minelli, G., Basara, B., Krajnović, S., 2018b. An LES investigation of the near wake of a simplified heavy vehicle. Flow, Turbul. Combust. https://doi.org/10.1007/s10494-018-9959-6.

Rigas, G., Esclapez, L., Magri, L., 2017. Symmetry breaking in a 3D bluff-body wake. ArXiv e-prints eprint = 1703.07405.

Robertson, E., Choudhury, V., Bhushan, S., Walters, D.K., 2015. Validation of OpenFOAM numerical methods and turbulence models for incompressible bluff body flows. Comput. Fluids 123, 122–145.

Rouméas, M., Gilliéron, P., Kourta, A., 2009. Analysis and control of the near-wake flow over a square-back geometry. Comput. Fluids 38, 60–70.

Roy, C., Payne, J., McWherter-Payne, M., 2006. RANS simulations of a simplified tractor/trailer geometry. J. Fluid Eng. 128, 1083–1089.

Sagaut, P., 2006. Large Eddy Simulation for Incompressible Flows: an Introduction. Scientific Computation. Springer.

Salari, K., Ortega, J., Castellucci, P., 2004. Computational prediction of aerodynamic forces for a simplified integrated tractor-trailer geometry. In: 34th AIAA Fluid Dynamics Conference and Exhibit. Fluid Dynamics and Co-located Conferences, American Institute of Aeronautics and Astronautics, pp. 1–53, 0.

Salim, S.M., Ong, K.C., 2013. Performance of RANS, URANS and LES in the Prediction of Airflow and Pollutant Dispersion. Springer Netherlands, Dordrecht, pp. 263–274.

Sans, J., Resmini, M., Brouckaert, J.F., Hiernaux, S., 2014. The impact of turbulence model and numerical scheme on the performance of a linear compressor cascade. In: Proceedings of ASME Turbo Expo 2014: Turbine Technical Conference and Exposition, GT2014, June 16 20, 2014, Düsseldorf, Germany, pp. 1–15.

Schmidt, H.J., Woszidlo, R., Nayeri, C.N., Paschereit, C.O., 2018. The effect of flow control on the wake dynamics of a rectangular bluff body in ground proximity. Exp. Fluid 59, 107.

Serre, E., Minguez, M., Pasquetti, R., Guilmineau, E., Deng, G.B., Kornhaas, M., Schäfer, M., Fröhlich, J., Hinterberger, C., Rodi, W., 2013. On simulating the turbulent flow around the Ahmed body: a French–German collaborative evaluation of LES and DES. Comput. Fluids 78, 10–23. LES of turbulence aeroacoustics and combustion.

Shur, M.L., Spalart, P.R., Strelets, M.K., Travin, A.K., 2008. A hybrid RANS-LES approach with delayed-DES and wall-modelled LES capabilities. Int. J. Heat Fluid Flow 29, 1638–1649.

Sitlani, M.P., Aung, K., 2006. Numerical Simulations on Aerodynamic Drag of Ground Transportation System (GTS) Model.

Spalart, P., Jou, W., Strelets, M., Allmaras, S., 1997. Comments of feasibility of LES for wings, and on a hybrid RANS/LES approach. In: International Conference on DNS/LES, Aug. 4-8, 1997, Ruston, Louisiana, pp. 137–147.

Spalart, P.R., Deck, S., Shur, M.L., Squires, K.D., Strelets, M.K., Travin, A., 2006. A new version of detached-eddy simulation, resistant to ambiguous grid densities. Theor. Comput. Fluid Dynam. 20, 181.

Speziale, C.G., 1997. Computing non-equilibrium turbulent flows with time-dependent RANS and VLES. In: Fifteenth International Conference on Numerical Methods in Fluid Dynamics. Springer, Berlin, Heidelberg, pp. 123–129.

Storms, B., Ross, J., Heineck, J., Walker, S., Driver, D., Zilliac, G., 2001. An Experimental Study of the Ground Transportation System (GTS) Model in the NASA Ames 7-by 10-ft Wind Tunnel. National Aeronautics and Space Administration, Ames Research Center, pp. 1–21.

Sweby, P.K., 1984. High resolution schemes using flux limiters for hyperbolic conservation laws. SIAM J. Numer. Anal. 21, 995–1011.

Trias, F.X., Lehmkuhl, O., Oliva, A., Pérez-Segarra, C.D., Verstappen, R.W.C.P., 2014. Symmetry-preserving discretization of Navier–Stokes equations on collocated unstructured grids. J. Comput. Phys. 258, 246–267.

Unaune, S.V., Sovani, S.D., Kim, S.E., 2005. Aerodynamics of a generic ground transportation system: detached eddy simulation. In: SAE Technical Paper. SAE International.

Varon, E., Eulalie, Y., Edwige, S., Gilotte, P., Aider, J.L., 2017. Control of the Chaotic Dynamics of a Turbulent 3D Wake available online.

Vaz, G., Pereira, F.S., Eça, L., 2015. On the prediction of shear-layer flows with RANS and SRS models. In: VI International Conference on Computational Methods in Marine Engineering, pp. 1–18.

Verma, S., Dewan, A., 2018. Partially–Averaged Navier–Stokes (PANS) approach for study of fluid flow and heat transfer characteristics in Czochralski melt. J. Cryst. Growth 481, 56–64.

Verstappen, R.W.C.P., Veldman, A.E.P., 2003. Symmetry-preserving discretization of turbulent flow. J. Comput. Phys. 187, 343–368.

Vidales, A.F.R., 2016. Air-wake Flow Dynamics on a Simplified Frigate Shape - an Experimental Study by Large-scale Tomographic PIV. Theses. Delft University of Technology.

Volpe, R., Devinant, P., Kourta, A., 2014a. Unsteady experimental characterization of the natural wake of a squareback Ahmed model. In: ASME 2014 4th Joint US-european Fluids Engineering Division Summer Meeting Collocated with the ASME 2014 12th International Conference on Nanochannels, Microchannels, and Minichannels. ASME. V01CT17A007–1–V01CT17A007–7.

Volpe, R., Devinant, P., Kourta, A., 2015. Experimental characterization of the unsteady natural wake of the full-scale square back Ahmed body: flow bi-stability and spectral analysis. Exp. Fluid 56, 99.

Volpe, R., Ferrand, V., Silva, A.D., Moyne, L.L., 2014b. Forces and flow structures evolution on a car body in a sudden crosswind. J. Wind Eng. Ind. Aerod. 128, 114–125.

Wang, S., Bell, J.R., Burton, D., Herbst, A.H., Sheridan, J., Thompson, M.C., 2017. The performance of different turbulence models (URANS, SAS and DES) for predicting high-speed train slipstream. J. Wind Eng. Ind. Aerod. 165, 46–57.

Waterson, N., Deconinck, H., 2007. Design principles for bounded higher-order convection schemes a unified approach. J. Comput. Phys. 224, 182–207.

Yamada, Y., Miyata, H., 1993. Computational study of large eddy structure of flows past bluff body and oceanic topography. Jpn. Shipbuild. Sco. Proc. 19–26, 1993.

Zhang, J., Minelli, G., Rao, A., Basara, B., Bensow, R., Krajnović, S., 2018. Comparison of PANS and LES of the flow past a generic ship. Ocean Eng. 165, 221–236.

Zhiyin, Y., 2015. Large-eddy simulation: past, present and the future. Chin. J. Aeronaut. 28, 11–24.